

WRF-Chem simulation of aerosol seasonal variability in the San Joaquin Valley

Longtao Wu¹, Hui Su¹, Olga V. Kalashnikova¹, Jonathan H. Jiang¹, Chun Zhao²,
Michael J. Garay¹, James R. Campbell³ and Nanpeng Yu⁴

1. Jet Propulsion Laboratory, California Institute of Technology, Pasadena, CA, USA

2. School of Earth and Space Sciences, University of Science and Technology of China,

Hefei, Anhui, China

3. Naval Research Laboratory, Monterey, CA, USA

4. University of California, Riverside, Riverside, CA, USA

Submitted to *Atmospheric Chemistry and Physics*

April, 2017

Copyright: © 2017 California Institute of Technology.

All rights reserved.

Corresponding author address: Longtao Wu, 4800 Oak Grove Dr., Pasadena, CA 91109
E-mail: Longtao.Wu@jpl.nasa.gov

18 Highlights:

- 19 1. The WRF-Chem simulation successfully captures aerosol variations in the cold season in the
20 San Joaquin Valley (SJV), but has poor performance in the warm season.
- 21 2. High resolution model simulation can better resolve inhomogeneous distribution of
22 anthropogenic emissions in urban areas, resulting in better simulation of aerosols in the cold
23 season in the SJV.
- 24 3. Observations show that dust is a major component of aerosols in the SJV, especially in the
25 warm season. Poor performance of the WRF-Chem model in the warm season is mainly due
26 to misrepresentation of dust emission and vertical mixing.

27 **Abstract**

28 WRF-Chem simulations of aerosol seasonal variability in the San Joaquin Valley (SJV),
29 California are evaluated by satellite and in-situ observations. Results show that the WRF-Chem
30 model successfully captures the distribution, magnitude and variation of SJV aerosols during the
31 cold season. However, aerosols are not well represented in the warm season. Aerosol simulations
32 in urban areas during the cold season are sensitive to model horizontal resolution, with better
33 simulations at 4 km resolution than at 20 km resolution, mainly due to inhomogeneous distribution
34 of anthropogenic emissions and better represented precipitation in the 4 km simulation. In rural
35 areas, the model sensitivity to grid size is rather small. Our observational analysis reveals that dust
36 is a primary contributor to aerosols in the SJV, especially during the warm season. Aerosol
37 simulations in the warm season are sensitive to parameterization of dust emission in WRF-Chem.
38 The GOCART (Goddard Global Ozone Chemistry Aerosol Radiation and Transport) dust scheme
39 produces very little dust in the SJV while the DUSTRAN (DUST TRANsport model) scheme
40 overestimates dust emission. Vertical mixing of aerosols is not adequately represented in the model
41 based on CALIPSO (Cloud-Aerosol Lidar and Infrared pathfinder Satellite Observation) aerosol
42 extinction profiles. Improved representation of dust emission and vertical mixing in the boundary
43 layer are needed for better simulations of aerosols during the warm season in the SJV.

44

45 **1. Introduction**

46 The San Joaquin Valley (SJV) in the southern portion of the California Central Valley is
47 surrounded by coastal mountain range to the west and the Sierra Nevada range to the east. With
48 cool wet winters and hot dry summers, the unique natural environment makes SJV one of the most
49 productive agricultural regions in the world (SJV APCD, 2012 and references therein). However,
50 SJV is also one of the most polluted regions in US due to its unique geographical location. Frequent
51 stagnant weather systems are conducive to air pollution formation, while the surrounding
52 mountains block air flow and trap pollutions. Large seasonal and spatial variation of aerosol
53 occurrence and distribution are observed in the SJV. Although significant progress made to
54 improving local air quality in past decades has been achieved through strong emission controls,
55 PM_{2.5} (particulate matter with diameter $\leq 2.5 \mu\text{m}$) concentrations in the SJV remain well above
56 the national ambient air quality standards (NAAQS) threshold of $12 \mu\text{g m}^{-3}$ on an annual basis and
57 $35 \mu\text{g m}^{-3}$ on daily basis, occurring mainly during the cold season. Improved understanding of the
58 aerosol variability and impacts is needed to provide further guidance for emission control strategies
59 in the SJV.

60 Air quality models are a useful tool to understanding the formation and evolution of
61 aerosols and their impacts on air quality, weather and climate. However, it is quite challenging to
62 accurately simulate aerosol properties (Fast et al., 2014). Fast et al. (2014) summarized the factors
63 contributing to the errors in regional-scale modeling of aerosol properties. They include 1)
64 emission sources; 2) meteorological parameterizations; 3) representation of aerosol chemistry; 4)
65 limited understanding of the formation processes of secondary organic aerosol (SOA); 5) spatial
66 resolution; and 6) boundary conditions.

67 As one of the advanced regional air quality models available presently to the community,
68 the Weather Research and Forecasting model with Chemistry (WRF-Chem) has been widely used
69 to study aerosols and their impacts on regional air quality, weather and climate (e.g., Misenis and
70 Zhang, 2010; Zhang et al., 2010; Zhao et al., 2010; 2013a, 2013b; 2014; Wu et al., 2011a, 2011b,
71 2013; Fast et al., 2012, 2014; Scarino et al., 2014; Tessum et al., 2015; Campbell et al., 2016; Hu
72 et al., 2016). For example, Fast et al. (2014) showed that WRF-Chem simulations at 4 km
73 horizontal resolution captured the observed meteorology and boundary layer structure over
74 California in May and June of 2010 and the spatial and temporal variations of aerosols were
75 reasonably simulated. Aerosol simulations by WRF-Chem are usually sensitive to both local
76 emission and long-range transport of aerosols from the boundary conditions provided by the global
77 Model for Ozone and Related chemical Tracers, version 4 (MOZART-4). With a similar model
78 set-up, Zhao et al. (2013b) conducted a one-year simulation at 12 km horizontal resolution and
79 found that the WRF-Chem model represented the observed seasonal and spatial variation of
80 surface particulate matter (PM) concentration over California. However, underestimation of
81 elemental carbon (EC) and organic matter (OM) were noticed in the model simulation, with weak
82 sensitivity to horizontal resolution.

83 In this study, we focus on simulating aerosol seasonal variability in the SJV, California
84 using similar model configurations as that used in Zhao et al. (2013b) and Fast et al. (2014). This
85 paper serves as the first step for future investigation of the aerosol impact on regional climate and
86 the water cycle in California. Previous studies have demonstrated that aerosols are better simulated
87 at higher model resolution (Misenis and Zhang et al., 2010; Qian et al., 2010; Stround et al., 2011;
88 Fountoukis et al., 2013). However, most regional climate studies are still performed with coarse
89 model resolutions (on the order of 10 km) due to the availability of computational resources. This

90 study will investigate the sensitivity of aerosol simulations to horizontal resolution and identify
91 optimal model physical choices for reasonable representation of aerosol variabilities in the SJV.

92 Another application of air quality modeling is to provide initial *a priori* fields for remote
93 sensing retrievals. The WRF-Chem model has been proposed as an input for retrieval algorithms
94 to be developed for the recently-selected NASA (National Aeronautics and Space Administration)
95 MAIA (Multi-Angle Imager for Aerosols) mission, which aims to map PM component
96 concentrations in major urban areas (including the SJV, a testbed for the MAIA retrieval algorithm
97 development). A significant challenge for aerosol remote sensing in retrieving spatial information
98 on specific aerosol types, especially near the surface, is caused by the lack of information on the
99 vertical distribution of aerosols in the atmospheric column and limited instrument sensitivity to
100 aerosol types over land. The WRF-Chem model will be used to provide near-real-time estimation
101 of particle properties, aerosol layer heights, and aerosol optical depths (AOD) to constrain the
102 instrument-based PM retrievals. A reasonable estimate of aerosol properties from WRF-Chem is
103 critical to ensuring retrieval speed and quality. Considering the sensitivity of WRF-Chem
104 simulations to various factors such as initial and boundary conditions, model parameterizations
105 and emission sources (e.g., Wu and Petty, 2010; Zhao et al., 2010, 2013a, 2013b; Wu et al., 2011a,
106 2015; Fast et al., 2014; Campbell et al., 2016; Morabito et al., 2016), careful model evaluations
107 are needed before the simulations can be used operationally for remote sensing retrievals. Thus,
108 this study is important for the development of MAIA retrieval algorithms, critical to the success
109 of the MAIA mission.

110 This paper is organized as follows. Section 2 describes observational datasets used for
111 model evaluation. Section 3 provides the description of the WRF-Chem model and experiment

112 setup. Model simulations and their comparison with observations are discussed in section 4.
113 Section 5 presents the conclusions.

114 **2. Observations**

115 **2.1 Column-integrated Aerosol Optical Properties**

116 AOD is a measure of column-integrated light extinction by aerosols and a proxy for total
117 aerosol loading in the atmospheric column. The Aerosol Robotic Network (AERONET) provides
118 ground measurements of AOD every 15 minutes during daytime under clear skies (Holben et al.,
119 1998), with an accuracy approaching ± 0.01 (Eck et al., 1999; Holben et al., 2001; Chew et al.,
120 2011). The monthly level 2.0 AOD product with cloud screening and quality control is used in this
121 study. Ångström exponent (AE) is an indicator of aerosol particle size. Small (large) AE values
122 are generally associated with large (small) aerosol particles (Ångström, 1929; Schuster et al.,
123 2006). The AE between $0.4 \mu\text{m}$ and $0.6 \mu\text{m}$ is derived from AERONET observed AODs, and is
124 used to evaluate the model-simulated AE. For comparison with simulated AOD, AERONET AOD
125 is interpolated to $0.55 \mu\text{m}$ from $0.50 \mu\text{m}$ and $0.675 \mu\text{m}$ using the AE. In the SJV, only one
126 AERONET station at Fresno, CA (36.79°N , 119.77°W) has regular observations throughout the
127 California water year 2013 (WY2013) from October 2012 to September 2013.

128 The Multiangle Imaging Spectroradiometer (MISR) (Diner et al., 1998) instrument
129 onboard the Terra satellite has provided global coverage of AOD once a week since December
130 1999. The standard MISR retrieval algorithm provides AOD observations at 17.6 km resolution
131 using 16×16 pixels of $1.1 \text{ km} \times 1.1 \text{ km}$ each. About 70% of MISR AOD retrievals are within 20%
132 of the paired AERONET AOD, and about 50% of MISR AOD falls within 10% of the AERONET
133 AOD, except in dusty and hybrid (smoke+dust) sites (Kahn et al., 2010). We use version 22 of
134 Level 3 monthly AOD product at 0.5° resolution in this study.

135 **2.2 Surface Mass Concentration**

136 Surface PM_{2.5} speciation and PM₁₀ (particulate matter with diameter ≤ 10 μm) data are
137 routinely collected by two national chemical speciation monitoring networks: Interagency
138 Monitoring of Protected Visual Environments (IMPROVE) and the PM_{2.5} National Chemical
139 Speciation Network (CSN) operated by Environmental Protection Agency (EPA) (Hand et al.
140 2011; Solomon et al., 2014). IMPROVE collects 24-h aerosol speciation every third day at mostly
141 rural sites since 1988. The same frequency of aerosol speciation dataset was collected at EPA CSN
142 sites in urban and suburban areas since 2000. The observed organic carbon is converted to OM by
143 multiplying by 1.4 (Zhao et al., 2013b; Hu et al., 2016). Some precursors of aerosol pollutions
144 (such as NO₂ and SO₂) are observed hourly by EPA (data available at:
145 https://aqhdr1.epa.gov/aqsweb/aqstmp/airdata/download_files.html) and are used in this study.
146 Selected IMPROVE and EPA CSN sites used in this study are shown in Figure 1a.

147 **2.3 Aerosol Extinction Profile**

148 The aerosol extinction coefficient profile reflects the attenuation of the light passing
149 through the atmosphere due to the scattering and absorption by aerosol particles as a function of
150 range. Version 3 Level 2 532 nm aerosol extinction profiles derived from Cloud-Aerosol Lidar
151 with Orthogonal Polarization (CALIOP) backscatter profiles collected onboard the Cloud-Aerosol
152 Lidar and Infrared Pathfinder Satellite Observation (CALIPSO) satellite are used (Omar et al.,
153 2009; Young and Vaughan, 2009). Seasonal mean profiles are derived for WY2013 based on the
154 methodology outlined in Campbell et al. (2012), whereby quality-assurance protocols are applied
155 to individual profiles before aggregating and averaging the data. We highlight that no individual
156 profiles are included in the averages if the CALIOP Level 2 retrieval failed to resolve any
157 extinction within the column, a potential issue to create bias that has recently been described by

158 Toth et al. (2017). Level 2 532 nm aerosol extinction data classify aerosols into 6 types: clean
159 marine, dust, polluted continental, clean continental, polluted dust and smoke. Dust and polluted
160 dust are distinguished in the averages in this study for their contribution to total extinction and the
161 vertical profile seasonally in the SJV.

162 **2.4 Meteorology**

163 AIRS (Atmospheric Infrared Sounder) onboard the Aqua satellite (Susskind et al., 2003;
164 Divakarla et al., 2006) has provided global coverage of the tropospheric temperature and moisture
165 at approximately 01:30 and 13:30 local time since 2002. AIRS retrievals have root-mean-squared
166 (RMS) error of ~1 K for temperature and ~15% for water vapor (Divakarla et al., 2006). Level 3
167 monthly temperature and moisture retrievals (version 6) at $1^\circ \times 1^\circ$ grid are used in this study.
168 Vertical gradient of equivalent potential temperature (θ_e) marks atmospheric stability and is
169 computed from temperature and moisture profiles observed by AIRS. Vertical profiles from the
170 European Center for Medium-Range Weather Forecasts Interim Re-Analysis (ERA-Interim; Dee
171 et al., 2011) are also used for comparison. Surface observations, including air temperature, relative
172 humidity (RH) and wind speed, are routinely collected at the California Irrigation Management
173 Information System (CIMIS; <http://www.cimis.water.ca.gov/>). Precipitation used in this study is
174 the Climate Prediction Center (CPC) Unified Gauge-Based Analysis of Daily Precipitation product
175 at $0.25^\circ \times 0.25^\circ$ resolution.

176 **3. Model Description and Experiment Setup**

177 The WRF-Chem model Version 3.5.1 (Grell et al., 2005) updated by Pacific Northwest
178 National Laboratory (PNNL) is used in this study (Zhao et al., 2014). This study uses the CBM-Z
179 (carbon bond mechanism) photochemical mechanism (Zaveri and Peters, 1999) coupled with the
180 sectional-bin MOSAIC (Model for Simulating Aerosol Interactions and Chemistry) aerosol

181 scheme (Zaveri et al., 2008) as the chemical driver. The major components of aerosols (nitrate,
182 ammonium, EC, primary OM, sulfate, sea salt, dust, water and other inorganic matter) as well as
183 their physical and chemical processes are simulated in the model. For computational efficiency,
184 aerosol particles in this study are partitioned into four-sectional bins with dry diameter within
185 0.039-0.156 μm , 0.156-0.625 μm , 0.625-2.5 μm , and 2.5-10.0 μm . Zhao et al. (2013a) compared
186 the impact of aerosol size partition on dust simulations. It showed that the 4-bin approach
187 reasonably produces dust mass loading and AOD compared with the 8-bin approach. The size
188 distribution of the 4-bin approach follows that of the 8-bin approach with coarser resolution,
189 resulting in $\pm 5\%$ difference on the ratio of $\text{PM}_{2.5}$ -dust/ PM_{10} -dust in dusty regions (more large
190 particles and less small particles). Dust number loading and absorptivity are biased high in the 4-
191 bin approach compared with the 8-bin approach.

192 Aerosols are considered to be spherical and internally mixed in each bin (Barnard et al.,
193 2006; Zhao et al., 2013b). The bulk refractive index for each particle is calculated by volume
194 averaging in each bin. Mie calculations as described by Ghan et al. (2001) are used to derive
195 aerosol optical properties (such as extinction, single-scattering albedo, and the asymmetry
196 parameter for scattering) as a function of wavelength. Aerosol radiation interaction is included in
197 the shortwave and longwave radiation schemes (Fast et al., 2006; Zhao et al., 2011). By linking
198 simulated cloud droplet number with shortwave radiation and microphysics schemes, aerosol
199 cloud interaction is effectively simulated in WRF-Chem (Chapman et al., 2009). Aerosol snow
200 interaction is implemented in this version of WRF-Chem (Zhao et al., 2014) by considering aerosol
201 deposition on snow and the subsequent radiative impacts through the SNICAR (SNow, ICe, and
202 Aerosol Radiative) model (Flanner and Zender, 2005, 2006).

203 The model simulations start on 1 September 2012 and run continuously for 13 months.
204 With the first month used for the model spin-up, our analysis focuses on WY2013 from October
205 2012 to September 2013. The model is configured with 40 vertical levels and a model top at 50
206 hPa. The vertical resolution from the surface to 1 km gradually increases from 28 m to 250 m. The
207 model center is placed at 38°N, 121°W, with 250 x 350 grid points at 4 km horizontal resolution
208 (referred to as “4km” hereafter; Table 1), covering California and the surrounding area. To test the
209 sensitivity of the aerosol simulations to horizontal resolution, one simulation with the same model
210 settings and domain coverage is conducted at 20 km horizontal resolution (referred to as “20km”
211 hereafter).

212 The physics parameterizations used in the simulations include the Morrison double-
213 moment microphysics scheme (Morrison et al., 2009), Rapid Radiative Transfer Model for General
214 circulation model (RRTMG) shortwave and longwave radiation schemes (Iacono et al., 2008),
215 Community Land Model (CLM) Version 4 land surface scheme (Lawrence et al., 2011). The
216 Yonsei University (YSU) planetary boundary layer (PBL) scheme (Hong et al., 2006) is used in
217 all of the simulations, except one sensitivity experiment that uses the ACM2 (Asymmetric
218 Convective Model with non-local upward mixing and local downward mixing; Pleim, 2007) PBL
219 scheme (referred to as “20km_P7” hereafter, Table 1). Previous studies showed that both YSU and
220 ACM2 schemes have good performance in simulating boundary layer properties (e.g., Hu et al.,
221 2010; Xie et al., 2012; Cuchiara et al., 2014; Banks and Baldasano, 2016; Banks et al., 2016; Chen
222 et al., 2017). Subgrid convection, convective transport of chemical constituents and aerosols, and
223 wet deposition from subgrid convection are parameterized using the Grell 3D ensemble cumulus
224 scheme (Grell and Devenyi, 2002) in the 20 km simulations while convective processes are
225 resolved in the 4 km simulations. The ERA-Interim reanalysis serves as initial and boundary

226 meteorological conditions for WRF-Chem. The MOZART-4 global chemical transport model
227 (Emmons et al., 2010) is used for initial and boundary chemical conditions. Fast et al. (2014) found
228 that the MOZART-4 model overestimates aerosols in the free troposphere over California, which
229 is also found in one of our sensitivity experiments (“20km_BC1” in the supplementary). Following
230 Fast et al. (2014), the chemical initial and boundary conditions from MOZART-4 are divided by
231 two in all simulations except 20km_BC1.

232 Anthropogenic emissions are provided by US EPA 2005 National Emissions Inventory
233 (NEI05), with area-type emissions on a structured 4-km grid and point-type emissions at specific
234 latitude and longitude locations (US EPA, 2010). Nineteen gases (including SO₂, NO, NH₃ etc.)
235 are emitted, and aerosol emissions include SO₄, NO₃, EC, organic aerosols, and total PM_{2.5} and
236 PM₁₀ masses. Anthropogenic emissions are updated every hour to account for diurnal variability,
237 while its seasonal variation is not considered in the simulations. A sensitivity experiment with
238 2011 NEI emissions (“20km_NEI11” in the supplementary) does not produce significantly
239 different results from the 2005 NEI emissions. Biogenic emissions are calculated online using the
240 Model of Emissions of Gases and Aerosols from Nature (MEGAN) model (Guenther et al., 2006).
241 Biomass burning emissions are obtained from the Global Fire Emissions Database version 2.1,
242 with eight-day temporal resolution (Randerson et al., 2007) and updated monthly. Sea salt
243 emissions are derived from the PNNL-updated sea salt emission scheme that includes the
244 correction of particles with radius less than 0.2 μm (Gong et al., 2003) and dependence on sea
245 surface temperature (Jaeglé et al., 2011).

246 Following Zhao et al. (2013b), dust emission is computed from the GOCART (Goddard
247 Global Ozone Chemistry Aerosol Radiation and Transport) dust scheme (Ginoux et al., 2001) in
248 the 20km and 4km simulations. The GOCART dust scheme estimates the dust emission flux F as

$$249 \quad F = CSs_p u_{10m}^2 (u_{10m} - u_t) \quad ,$$

250 where C is an empirical proportionality constant, S is a source function for potential wind erosion
 251 that is derived from 1° x 1° GOCART database (Freitas et al., 2011), s_p is a fraction of each size
 252 class dust in emission, u_{10m} is 10-m wind speed and u_t is a threshold speed for dust emission.

253 As shown later, a significant amount of dust is observed in the SJV, whereas the GOCART
 254 dust scheme produces little dust. Two sensitivity experiments at 20 km and 4 km horizontal
 255 resolution (hereafter referred to as “20km_D2” and “4km_D2”, respectively) are conducted by
 256 switching the dust emission scheme to the DUST TRANsport model (DUSTRAN) scheme (Shaw
 257 et al., 2008). The DUSTRAN scheme estimates F as

$$258 \quad F = \alpha C u_*^4 \left(1 - \frac{f_w u_{*t}}{u_*}\right) \quad ,$$

259 where C is an empirical proportionality constant, α is the vegetation mask, u_* is the friction
 260 velocity, u_{*t} is a threshold friction velocity and f_w is the soil wetness factor. The C value in both
 261 GOCART and DUSTRAN is highly tunable for different regions. The original C values, $1.0 \mu\text{g s}^2$
 262 m^{-5} in GOCART (Ginoux et al., 2001) and $1.0 \times 10^{-14} \text{ g cm}^{-6} \text{ s}^{-3}$ in DUSTRAN (Shaw et al., 2008),
 263 are used in this study.

264 **4. Model Simulation Results**

265 Shown in Fig. 1a, our model domain includes three urban sites (Fresno, Bakersfield and
 266 Modesto) and two rural sites (Pinnacles and Kaiser) where surface measurements of aerosols are
 267 available. Because aerosols properties and model performance are similar at all urban sites, our
 268 discussion is focused on the results at Fresno and the simulations for other urban sites are provided
 269 in the supplementary materials. Model simulations in the rural areas are presented in the last
 270 subsection.

271 **4.1 Sensitivity to Horizontal Resolution**

272 Figure 1 features daily mean anthropogenic $PM_{2.5}$ emission rates used in the 20km and
273 4km simulations, respectively. Although both emission rates are derived from the 4 km NEI05
274 dataset, localized high emission rates with sharp gradients are evident in urban areas from the 4km
275 simulation (Fig. 1b). The 20km simulation exhibits lower emission rates at the urban areas with
276 weaker gradients due to the reapportionment process (Fig. 1a). As precipitation is an important
277 process that removes aerosols, we examine the simulated precipitation for the 20km and 4km runs
278 and find that the 20km simulation produces 51% more precipitation, although the domain averaged
279 precipitation is lower in the 20km run than the 4km run (Fig. 2a).

280 Consistent with higher emission rates and lower precipitation at Fresno, the 4km run
281 simulates higher AOD than the 20km run in the cold season (October-November-December and
282 January-February-March; OND and JFM in Fig. 3). Averaged over a broad area encompassing
283 Fresno and Bakersfield, the most polluted region in the SJV (red box in Fig. 1a), the AOD is 0.090
284 in the 4km and 0.073 in the 20km, a 23% difference. Compared to the MISR observations, the
285 4km simulation reproduces the spatial distribution and magnitude of AOD in the cold season.
286 However, the AOD difference between the 20km and 4km runs is small in the warm season (April-
287 May-June and July-August-September; AMJ and JAS in Fig. 3), and both runs underestimate AOD
288 by ~50% with respect to the MISR observations.

289 Comparing the point values at Fresno in the 4km and 20km simulations (Fig. 4a), we find
290 similar results: the 4km AOD is closer to the AERONET measurements and is about 23% higher
291 than that in the 20km run during the cold season, while both runs are biased low in AOD during
292 the warm season. The different model sensitivities to horizontal resolution between the cold and
293 warm seasons suggest that the dominant aerosol sources may be different for the two seasons. We
294 will elaborate upon the aerosol composition in the following section. MISR and AERONET

295 observations display weak seasonal AOD variation in the SJV and at Fresno, respectively, which
296 is not well represented in the 20km and 4km simulations (Fig. 3 and 4a).

297 Aside from AOD, significant seasonal variability of AE (Fig. 4b) is shown at Fresno. AE
298 exhibits a maximum about 1.50 in January and a minimum of 0.98 in April, suggesting relatively
299 small particles in the winter and large particles in the spring. A relatively large AE value of 1.40
300 (corresponding to small particles) is observed in July, possibly related to the wild fires in late July
301 in the SJV. WRF-Chem captures the seasonal variability of the AE well, with a correlation of 0.90
302 in both the 20km and 4km simulations. The magnitude of AE is also approximately simulated in
303 the cold season, with a mean of 1.15 (1.20) in the 20km (4km) runs compared to 1.33 in the
304 observation. However, the simulated AE is underestimated by ~30% in the warm season,
305 indicating that the simulated particle size is biased high during this period.

306 Significant seasonal variability of $PM_{2.5}$ is observed in the SJV urban areas (Fig. 5a and
307 Supplementary Fig. 4a and 5a). $PM_{2.5}$ at Fresno peaks in January ($26.18 \mu\text{g m}^{-3}$) and reaches a
308 minimum of $7.03 \mu\text{g m}^{-3}$ in June, with an annual nonattainment value of $12.64 \mu\text{g m}^{-3}$ (Fig. 5a).
309 Both the 20km and 4km runs approximately capture the observed seasonal variability of $PM_{2.5}$,
310 with a correlation around 0.90 (Table 2). In the cold season, the 4km simulation overestimates
311 $PM_{2.5}$ by 27% while the 20km simulation exhibits a low bias of 19% compared with IMPROVE
312 observations at Fresno (Table 3). The 4km simulation of PM_{10} is in good agreement with
313 IMPROVE in the winter (December, January and February), but has significant low biases of
314 between 30% and 85% in other months (Fig. 5b). The 20km simulation underestimates PM_{10}
315 throughout WY2013.

316 $PM_{2.5}$ is a mixture of nitrate (NO_3), ammonia (NH_4), OM, EC, sulfate (SO_4), dust and other
317 aerosols. High concentrations of $PM_{2.5}$ are primarily the result of NO_3 at Fresno (Fig. 5c). Both

318 simulations produce the seasonal variability of NO_3 with a correlation of 0.94, but high bias of 17%
319 (75%) is found in the 20km (4km) simulations during the cold season. As one precursor of NO_3 ,
320 NO_2 is underestimated by 43% in the 20km run (Fig. 6a). The overestimation in NO_3 and
321 underestimation in NO_2 suggest that the precursor emissions may not be the reason for the high biases
322 in NO_3 . NH_4 shows a similar performance to NO_3 , with an overestimation by 38% (111%) in the
323 20km (4km) runs during the cold seasons (Fig. 5d). As shown later in section 4.3, both NO_3 and
324 NH_4 simulations are quite sensitive to the PBL scheme applied.

325 OM, the second largest contributing species to cold season $\text{PM}_{2.5}$ in the SJV (Table 3), is
326 significantly underestimated by 82% in the 20km simulation (Fig. 5f). The 4km simulation
327 produces higher OM, but it is still lower than the IMPROVE observations by 63%. The
328 underestimation of OM is expected, because SOA processes are not included in our model
329 infrastructure. Fast et al. (2014) used the simplified two-product volatility basis set
330 parameterization to simulate equilibrium SOA partitioning in WRF-Chem although SOA was still
331 underestimated in their simulation. It remains ongoing research how to correctly represent SOA
332 processes in regional climate models.

333 Both the 20km and 4km simulations reproduce the seasonal variability of EC, with a
334 correlation of 0.98 between the modeled and observed time series (Table 2). The 20km simulation
335 underestimates EC by 52% (16%) in the cold (warm) season (Fig. 5e and Table 3). The 4km
336 simulated EC ($1.12 \mu\text{g m}^{-3}$) exhibits good agreement with IMPROVE ($1.08 \mu\text{g m}^{-3}$) in the cold
337 season, but overestimates EC by 53% in the warm season.

338 The seasonal variability of SO_4 at Fresno is very different from other $\text{PM}_{2.5}$ species. It peaks
339 in May at $1.35 \mu\text{g m}^{-3}$ and reaches the minimum of $0.67 \mu\text{g m}^{-3}$ in August (Fig. 5g). The 20km
340 simulated SO_4 exhibits good correlation of 0.63 with the observation (Table 2), but is biased low

341 by 28% to 63% throughout WY2013 (Fig. 5g). Although the observed SO₂, the precursor of SO₄,
342 has approximately similar seasonal variation to the observed SO₄ (Fig. 6b), the 20km simulated
343 seasonal variability of SO₂ resembles other anthropogenic emissions, with high values in the cold
344 season and low values in the warm season, out of phase with the simulated SO₄ and the observed
345 SO₂. The 4km simulation produces higher SO₄ than the 20km run, resulting in better agreement
346 with the observation (0.82 μg m⁻³ vs. 0.87 μg m⁻³) during the cold season (Fig. 5g and Table 3).
347 However, the 4km run produces an increase of SO₄ by only 13% comparing to the 20km run in
348 the warm season, resulting in a correlation of -0.16 between the 4km simulation and the
349 observation.

350 To explore the possible cause for the underestimation of SO₄ and SO₂ in the warm season
351 in both the 20km and 4km simulations, we conduct a sensitivity experiment with different chemical
352 boundary conditions from the baseline runs (20km_BC1 in the supplementary). We find that SO₄
353 in the SJV is partly contributed to by marine intrusions (the different chemical boundary conditions
354 between 20km_BC1 and 20km_D2) throughout the year (supplementary Fig. 2g), as pointed out
355 by Fast et al. (2014). Including the marine intrusions, the 20km_BC1 simulated SO₄ tracks the
356 observation at a correlation of 0.78. Doubled chemical boundary conditions in the 20km simulation
357 results in 41% increase in SO₄ at Fresno, with a stronger increase in the warm season. Compared
358 to the observed SO₄ of 1.04 μg m⁻³ in the warm season, the simulated SO₄ of 0.79 μg m⁻³ in the
359 20km_BC1 run is closer to the observation than that simulated in the 20km_D2 run (0.53 μg m⁻³).
360 The relative contributions of local emissions and remote transports (as well as other emission
361 sources, such as wild fires) to SO₄ concentrations in different seasons of the SJV require further
362 investigation.

363 Overall, the 4km simulation produces higher AOD and surface PM than the 20km
364 simulation in urban areas of the SJV, especially during the cold season, resulting in better
365 agreement with satellite and surface observations than the 20km simulation. Both the 20km and
366 4km simulations approximately capture the seasonal variability of $PM_{2.5}$ and most of its speciation.
367 However, significant low biases of AOD and PM_{10} are found during the warm season in both
368 simulations. The underestimation also exists in a sensitivity experiment (not shown) with the same
369 model setups except initialized in April, indicating that the identified model biases during the warm
370 season are not caused by potential model drift after a relatively long simulation period. The
371 relatively good performance in simulating $PM_{2.5}$ but not PM_{10} during the warm season suggests
372 that coarse aerosol particle mass (CM; $10 \mu m \geq$ particulate matter with diameter $> 2.5 \mu m$), mainly
373 dust in the SJV, is not properly represented in the model. The impact of dust parameterizations is
374 investigated in the 4km_D2 experiment.

375 **4.2 Sensitivity to Dust Scheme**

376 Limited amounts of $PM_{2.5_dust}$ (dust with diameter $\leq 2.5 \mu m$) are observed in the SJV cold
377 season, with a minimum of $0.37 \mu g m^{-3}$ in December (Fig. 7a). The amount of $PM_{2.5_dust}$ increases
378 in the warm season, with a peak of $3.86 \mu g m^{-3}$ in September. The 4km simulation produces
379 comparable $PM_{2.5_dust}$ relative to IMPROVE in the winter, but almost no dust in other months
380 (Fig. 7 and upper panel in Fig. 8). On the other hand, the dust emission rate in the 4km_D2 run is
381 significantly higher than the 4km run. We have found that the source function, S , for potential
382 wind erosion in the SJV is set to zero in the $1^\circ \times 1^\circ$ GOCART dataset used for the 4km simulation
383 (Fig. 9). An updated source function, S , at higher resolution is needed for the GOCART dust
384 scheme to correctly represent dust emissions in the SJV.

385 The 4km_D2 simulation reproduces the amount of PM_{2.5_dust} in OND (Fig. 7a). However,
386 it overestimates PM_{2.5_dust} by up to a factor of 3 in the warm season, resulting in an overestimation
387 of PM_{2.5} by 52% (Fig. 7b and Table 3). PM_{2.5_dust} is not sensitive to long-range transport (from
388 chemical boundary conditions in the model simulation; Supplementary Fig. 2h). Both the 4km and
389 4km_D2 simulations capture the seasonal variability of PM_{2.5}, but not that of PM₁₀ (Fig. 7c). The
390 magnitude of PM₁₀ in the 4km_D2 run is larger than the 4km simulation. PM₁₀ in the 4km_D2 run
391 is overestimated in April-May-June (AMJ) but underestimated in July-August-September (JAS),
392 leading to a comparable season mean of 38.12 $\mu\text{g m}^{-3}$ with IMPROVE observed 34.82 $\mu\text{g m}^{-3}$. The
393 overestimation of AMJ PM₁₀ and PM_{2.5_dust} in the 4km_D2 run is likely associated with the high
394 bias in the simulated wind speed (Fig. 2b).

395 On the relative contribution of different aerosol species, IMPROVE observations at Fresno
396 show that NO₃ is the primary contributor (32.3%) to PM_{2.5} while only 5.3% of PM_{2.5} is dust in the
397 cold season (panel 1 of Fig. 10). Both the 4km and 4km_D2 runs roughly reproduce the relative
398 contributions to PM_{2.5} in the cold season, with an overestimation of NO₃ and NH₄ and an
399 underestimation of OM, consistent with the time series in Fig. 5. Relative contributions of dust to
400 PM_{2.5} are better simulated in the 4km_D2 run (7.3%) than the 4km one (<1.0%). IMPROVE shows
401 that 46.6% of PM₁₀ is CM in the cold season (panel 2 of Fig. 10). Both the 4km (6.3%) and
402 4km_D2 (20.6%) runs underestimate the contribution of CM to PM₁₀, mainly in October and
403 November. In the warm season, dust (24.6%) becomes the primary contributor to PM_{2.5} while the
404 contribution from NO₃ decreases to 9.9% in IMPROVE observations (panel 3 of Fig. 10). Almost
405 no PM_{2.5_dust} is simulated in the 4km run while too much PM_{2.5_dust} is produced in the 4km_D2
406 (50.5%) run during the warm season. The relative contribution of CM to PM₁₀ is too small (27.6%)

407 in the 4km run, while the 4km_D2 run reflects a better relative contribution of 66.3% as compared
408 to an IMPROVE observed 75.8% (panel 4 of Fig. 10).

409 AOD simulations are improved in the 4km_D2 experiment (Fig. 11), with better agreement
410 found from MISR (Fig. 3) in AMJ. AOD (0.114) in the 4km_D2 run is comparable to observations
411 (0.131) in AMJ, but still underestimated by 53% in JAS. Consistent with AOD, the vertical
412 distribution of aerosol extinction is reasonably simulated during the cold season in the WRF-Chem
413 simulations, while large discrepancies are found in the warm season (Fig. 12). As observed by
414 CALIOP at 532 nm, aerosols are confined below 1 km in the cold season and decrease sharply
415 with height. During AMJ, aerosols are well mixed between the surface and the altitude of 1.5 km
416 and then decrease with height gradually. During JAS, the well-mixed aerosol layer is shallower
417 than that in AMJ and the vertical profile of aerosol extinction is in-between the cold season and
418 AMJ. Model simulations roughly capture the “bottom-heavy” structure of the extinction profiles
419 observed by CALIOP especially in the cold season, but significant biases exist. One common
420 problem for all four seasons is the low bias in the boundary layer and high bias in the free
421 atmosphere. Similar discrepancy between the model simulations and CALIOP is shown in other
422 studies (Wu et al., 2011a; Hu et al., 2016). The model does not capture the well-mixed aerosol
423 layer during AMJ. The difference in the aerosol extinction profiles between the 4km and 4km_D2
424 runs is small during the cold season.

425 Dust in the boundary layer is a primary factor contributing to aerosol extinction in the SJV,
426 as illustrated by the differences between the bulk seasonal CALIOP mean profile and those
427 excluding the contributions of the dust and polluted dust (CALIOP_nodust) profiles (Fig. 12).
428 Simulated aerosol extinction falls between the two in all seasons, suggesting that dust is the
429 primary factor contributing to the model biases in aerosol extinction. Although a small portion of

430 $PM_{2.5}$ is dust in the cold season, it contributes to about 50% of total aerosol extinction (Fig. 12a
431 and 12b). A predominant portion of aerosol extinction in the lower troposphere is contributed by
432 dust in the warm season (Fig. 12c and 12d). There, the 4km_D2 simulation produces higher aerosol
433 extinction between 0.3 km and 3 km than the 4km simulation, although it is still lower than
434 CALIOP. The simulated aerosol extinction in the free troposphere is close to or larger than
435 CALIOP, suggesting that aerosols transported from remote areas through chemical boundary
436 conditions (e.g., the differences between the 20km_BC1 and 20km_D2 runs in Supplementary Fig.
437 3) may not be the major factor contributing to the underestimation of dust between 0.3 km and 3
438 km in the SJV.

439 Overall, the poor simulations of dust play a dominant role in the low bias of aerosols in
440 the boundary layer during the warm season. Both the GOCART and DUSTRAN dust emission
441 schemes used in this study have difficulties in reproducing dust emissions in the SJV, with an
442 underestimation in GOCART and an overestimation in DUSTRAN (Fig. 7). Improvement on the
443 dust emission schemes is needed for capturing the seasonal variability of aerosols in the SJV.

444 **4.3 The Role of Meteorology**

445 The WRF-Chem simulations approximately reproduce the seasonal variations of
446 meteorological variables near the surface (correlations > 0.80), including temperature, RH, wind
447 speed and precipitation (Supplementary Fig. 6 and Supplementary Table 1). All of the model
448 simulations exhibit warm and dry biases near surface and in the boundary layer, with cold and wet
449 biases in the free atmosphere (Supplementary Fig. 6-8 and Supplementary Table 2). The dry bias
450 in the 4km_D2 run is about 10% near the surface throughout WY2013. Due to the relative dry
451 environment ($RH < 50\%$) in the warm season, the underestimation of boundary layer aerosol
452 extinction and column-integrated AOD is unlikely caused by the hygroscopic effects (Feingold

453 and Morley, 2003). In the cold season, the surface wind speed is underestimated by 0.67 m s^{-1}
454 (1.00 m s^{-1}) in the 4km_D2 (20km_D2) runs. In the warm season, the 4km_D2 run overestimates
455 wind speed by 0.78 m s^{-1} , while the 20km_D2 run has an underestimation of 0.16 m s^{-1} . These
456 results suggest that wind speed is not a major factor contributing to the low biases of aerosols in
457 the boundary layer between 0.3 km and 3 km. Furthermore, the seasonal variability of
458 precipitation is well captured in the simulations, while the magnitude of precipitation is weaker
459 than the observations during the warm season (Supplementary Table 2). Thus, we conclude that
460 wet removal processes would not be a primary reason for the aerosol biases in the warm season.

461 In the warm season, more aerosols are observed above 1.5 km than in the cold season (Fig.
462 12). A well-mixed layer of aerosols is observed below 1.5 km in AMJ (Fig. 12c), consistent with
463 the unstable lower troposphere below 1.5 km shown in AIRS and ERA-Interim (Fig. 13c). The
464 WRF-Chem model simulates neutral (or weakly stable) layers below 1.5 km, which may limit
465 uplifting of aerosols from the surface, failing to create a deep well-mixed layer of aerosols (Fig.
466 12c). Although the dust emission at the surface is overestimated in AMJ in the 4km_D2 run, the
467 simulated neutral or weakly stable thermal structure does not favor convective vertical mixing,
468 resulting in the low biases of aerosols between 0.3 km and 3 km.

469 Similar biases of aerosol and instability in the lower troposphere are also shown in JAS
470 (Fig. 12d and 13d). The stable boundary layer limits vertical transport of aerosols from the surface,
471 contributing to the low bias of column-integrated AOD in JAS (Fig. 11). In JAS (Fig. 12d), aerosol
472 extinction close to the CALIOP observation is simulated in the free atmosphere, suggesting that
473 the low bias in AOD is not due to the halved chemical boundary conditions from MOZART-4. In
474 the cold season, in spite of some discrepancies in the magnitude of atmospheric stability, all of the

475 simulations capture the stable lower troposphere (Fig. 13a and 13b), consistent with relatively
476 good performance of aerosol simulations in the cold season.

477 As biases in the model simulations are found mainly within the boundary layer, a sensitivity
478 experiment is conducted at 20 km resolution using the ACM2 PBL scheme (20km_P7). Although
479 the changes in the meteorological variables (Supplementary Fig. 6-9) and atmospheric static
480 stability (Fig. 13) are rather small, the simulated surface NO_3 and NH_4 in the 20km_P7 run
481 decrease by 50% compared to the 20km_D2 run (Fig. 14c, 14d and Table 3). Considering that
482 more NO_3 and NH_4 are simulated at 4 km resolution than at 20 km resolution as shown in section
483 4.1, the use of the ACM2 PBL scheme at 4 km simulation would largely resolve the high biases
484 of NO_3 and NH_4 in the 4km_D2 simulation. The decrease of NO_3 and NH_4 near the surface is
485 because more aerosols are transported to the layers above 0.5 km (Fig. 15a and 15b), possibly
486 resulting from different convective vertical mixing in the PBL schemes. However, $\text{PM}_{2.5_dust}$ is
487 significantly overestimated by a factor of 4 in the 20km_P7 simulation (Fig. 14h), leading to a
488 small decrease of $\text{PM}_{2.5}$ by only 8% compared with the 20km_D2 run in the cold season. In the
489 warm season, $\text{PM}_{2.5_dust}$ in the 20km_P7 run is overestimated by a factor of 5, causing an
490 overestimation of $\text{PM}_{2.5}$ and PM_{10} (Fig. 14a and 14b). Aerosol extinctions in the boundary layer
491 above the surface increase in the warm season (Fig. 15c and 15d), possibly related to
492 overestimation of dust emissions and more conducive convective vertical transport in the PBL
493 scheme.

494 In summary, the WRF-Chem model captures the seasonal variations of meteorological
495 variables (temperature, RH, wind speed and precipitation), despite some deviations in magnitude.
496 The low biases in aerosol optical properties of the warm season likely do not originate from
497 hygroscopic effects, wet removal processes or dust emissions associated with the wind speed bias.

498 The model simulates a stable environment in the warm season, which is opposite to the observed
499 unstable environment. The simulated stable environment may be most likely responsible for low
500 biases in the aerosol extinction above the surface (0.3-3 km) and the column-integrated AOD in
501 the warm season. Switching to the ACM2 PBL scheme leads to improved vertical displacement of
502 aerosols in the boundary layer, thus an improvement in the simulations of NO_3 and NH_4 in the cold
503 season. However, dust emissions are significantly overestimated with the ACM2 PBL scheme,
504 which contributes partly to the better simulation of aerosol extinction in the boundary layer and
505 AOD in the column. These results highlight that improving the simulation of boundary layer
506 structure and processes are critical for capturing the vertical profiles of aerosol extinction.

507 **4.4 Results in Rural Areas**

508 In general, low values of PM concentration are observed in the rural areas, Pinnacles and
509 Kaiser (Fig. 16 and 17). The rural areas share some similar model performance to the urban areas,
510 such as the overestimation of NO_3 , reasonable simulation of EC, good representation of SO_4 in the
511 cold season and underestimation of SO_4 in the warm season. However, the results are not sensitive
512 to model resolution. It suggests that high resolution is particularly important for heavily polluted
513 areas due to the inhomogeneity of emission sources, but less important for relatively lightly
514 polluted areas.

515 In late July/early August, MODIS (Moderate Resolution Imaging Spectroradiometer) fire
516 data (not shown) showed active wild fires close to Kaiser, which resulted in high concentration of
517 aerosols locally (Fig. 17). Our model simulations with monthly-varying fire emissions fail to
518 reproduce these fire events. Previous studies (e.g., Grell et al., 2011; Wu et al. 2011a; Archer-
519 Nicholls et al., 2015) demonstrated that the WRF-Chem model can capture aerosols distributions
520 from wild fires based on fire locations from satellite observations. Campbell et al. (2016) further

521 described the difficulties in constraining total aerosol mass from operational satellite fire
522 observations and the time needed by the model for diffusion within the near-surface layers to
523 render both reasonable AOD and vertical profiles of aerosol extinction. For operational application
524 of the WRF-Chem model in MAIA retrievals, the observations of daily fire events need to be more
525 appropriately considered.

526 **5. Summary**

527 The WRF-Chem (Weather Research and Forecasting model with Chemistry) model is
528 employed to simulate the seasonal variability of aerosols in WY2013 (water year 2013) in the SJV
529 (San Joaquin Valley). Model simulations are evaluated using satellite and in-situ observations. In
530 general, the model simulations conducted at 4 km resolution reproduce the spatial and temporal
531 variations of regional aerosols in the cold season, when aerosols are mainly contributed to by
532 anthropogenic emissions in the SJV. The magnitude of simulated aerosols in the cold season
533 however, especially in relatively dense urban areas, is sensitive to model horizontal resolution.
534 The 4km simulation has comparable magnitude to available observations, while the 20km
535 simulation underestimates aerosols. Differences in aerosol simulation fidelity as a function of
536 variable resolutions are mainly due to the difference in aerosol emissions and simulated
537 precipitation. Emissions at higher resolution can better resolve the inhomogeneity of
538 anthropogenic emissions in the SJV than at lower resolution. The sensitivity to horizontal
539 resolution is small in rural areas and during warm season, where/when the relative contribution of
540 anthropogenic emissions is small.

541 Previous studies in the SJV are mainly focused on PM_{2.5} (particulate matter with diameter
542 $\leq 2.5 \mu\text{m}$) and during cold season (e.g. Chow et al., 2006; Herner et al., 2006; Pun et al., 2009;
543 Ying and Kleeman, 2009; Zhang et al., 2010; Chen et al., 2014; Hasheminassab et al., 2014; Kelly

544 et al., 2014; Baker et al., 2015; Brown et al., 2016). CALIOP (Cloud-Aerosol Lidar with
545 Orthogonal Polarization) and IMPROVE (Interagency Monitoring of Protected Visual
546 Environments) observations show that dust is a primary contributor to the aerosols in the SJV,
547 especially in the warm season. Dust contributes 24.6% to $PM_{2.5}$ while more than 75.8% to PM_{10} in
548 the warm season. For all seasons, the major component of aerosol extinction in the boundary layer
549 is dust as observed by CALIOP, consistent with Kassianov et al. (2012). For a complete
550 understanding of aerosol impacts on air quality, weather and climate, the full spectrum of aerosols
551 should be considered during all seasons.

552 All the model simulations conducted fail to capture aerosol vertical distribution and
553 variability in the SJV warm season, largely due to the misrepresentation of dust emissions, static
554 stability and vertical mixing in the boundary layer. The GOCART (Goddard Global Ozone
555 Chemistry Aerosol Radiation and Transport) dust emission scheme significantly underestimates
556 dust due to the non-active source function, S , for potential wind erosion used in this study while
557 the DUSTRAN (DUST TRANsport model) scheme may overestimate dust emission in the SJV.
558 Along with the bias in dust emissions, our simulations produce a relatively stable boundary layer
559 in the warm season, in contrast with observations suggesting a more unstable environment, leading
560 to a weak vertical mixing of aerosols in the boundary layer. Improved dust emission and better
561 simulations of the boundary layer properties are needed for accurate simulation of aerosols in the
562 SJV warm season.

563 Other biases are also identified in the model simulations. NO_3 and NH_4 in the cold season
564 are overestimated in the model, but the results are sensitive to the choice of the PBL (planetary
565 boundary layer) scheme. The SOA (secondary organic aerosol) processes contribute to the
566 underestimation of OM (organic matter) in this study. The underestimation of sulfate in the warm

567 season may be caused by the misrepresentation of emissions and the chemical boundary conditions
568 related to marine intrusions. Aerosols from wild fires are not captured in the simulations with
569 monthly updated fire data. Further investigations are needed to improve model simulations in the
570 SJV for both scientific and operational applications.

571 **Acknowledgements**

572 This study was carried out at the Jet Propulsion Laboratory, California Institute of
573 Technology, under a contract with the National Aeronautics and Space Administration. The
574 authors thank the funding support from the NASA ACMAP program and JPL PDF program. This
575 work is partially sponsored by California Energy Commission under grant #EPC-14-064. Author
576 JRC acknowledges the support of the NASA ACCDAM program and its manager Hal Maring.
577 The authors thank the three anonymous reviewers for their helpful comments.

578 **References**

- 579 Archer-Nicholls, S., Lowe, D., Darbyshire, E., Morgan, W. T., Bela, M. M., Pereira, G., Trembath,
580 J., Kaiser, J. W., Longo, K. M., Freitas, S. R., Coe, H., and McFiggans, G.: Characterising
581 Brazilian biomass burning emissions using WRF-Chem with MOSAIC sectional aerosol,
582 *Geosci. Model Dev.*, 8, 549-577, doi:10.5194/gmd-8-549-2015, 2015.
- 583 Ångström, A.: On the atmospheric transmission of Sun radiation and on dust in the air, *Geogr.*
584 *Ann.*, 11, 156–166, 1929.
- 585 Baker, K. R., Carlton, A. G., Kleindienst, T. E., Offenberg, J. H., Beaver, M. R., Gentner, D. R.,
586 Goldstein, A. H., Hayes, P. L., Jimenez, J. L., Gilman, J. B., de Gouw, J. A., Woody, M. C.,
587 Pye, H. O. T., Kelly, J. T., Lewandowski, M., Jaoui, M., Stevens, P. S., Brune, W. H., Lin, Y.-
588 H., Rubitschun, C. L., and Surratt, J. D.: Gas and aerosol carbon in California: comparison of
589 measurements and model predictions in Pasadena and Bakersfield, *Atmos. Chem. Phys.*, 15,
590 5243-5258, doi:10.5194/acp-15-5243-2015, 2015.

- 591 Banks, R.F., Baldasano, J.M.: Impact of WRF model PBL schemes on air quality simulations over
592 Catalonia, Spain. *Science of the Total Environment*, 572, 98-113,
593 <http://dx.doi.org/10.1016/j.scitotenv.2016.07.167>, 2016.
- 594 Banks, R. F., Tiana-Alsina, J., Baldasano, J. M., Rocadenbosch, F., Papayannis, A., Solomos, S.,
595 and Tzanis, C. G.: Sensitivity of boundary-layer variables to PBL schemes in the WRF model
596 based on surface meteorological observations, lidar, and radiosondes during the HygrA-CD
597 campaign, *Atmos. Res.*, 176, 185–201, 2016.
- 598 Barnard, J. C., Fast, J. D., Paredes-Miranda, G., Arnott, W. P., and Laskin, A.: Technical Note:
599 Evaluation of the WRF-Chem “Aerosol Chemical to Aerosol Optical Properties” Module using
600 data from the MILAGRO campaign, *Atmos. Chem. Phys.*, 10, 7325–7340, doi:10.5194/acp-
601 10-7325-2010, 2010.
- 602 Brown, S. G., Hyslop, N. P., Roberts, P. T., McCarthy, M. C., and Lurmann, F. W.: Wintertime
603 vertical variations in particulate matter (PM) and precursor concentrations in the San Joaquin
604 Valley during the California Regional Coarse PM/Fine PM Air Quality Study, *J. Air Waste
605 Manage.*, 56, 1267–1277, 2006.
- 606 Campbell, J. R., Tackett, J. L., Reid, J. S., Zhang, J., Curtis, C. A., Hyer, E. J., Sessions, W. R.,
607 Westphal, D. L., Prospero, J. M., Welton, E. J., Omar, A. H., Vaughan, M. A., and Winker, D.
608 M.: Evaluating nighttime CALIOP 0.532 μm aerosol optical depth and extinction coefficient
609 retrievals, *Atmos. Meas. Tech.*, 5, 2143-2160, doi:10.5194/amtd-5-2143-2012, 2012.
- 610 Campbell, J. R., Ge, C., Wang, J., Welton, E. J., Bucholtz, A., Hyer, E. J., Reid, E. A., Chew, B.
611 N., Liew, S.-C., Salinas, S. V., Lolli, S., Kaku, K. C., Lynch, P., Mahmud, M., Mohamad, M.,
612 and Holben, B. N.: Applying Advanced Ground-Based Remote Sensing in the Southeast Asian
613 Maritime Continent to Characterize Regional Proficiencies in Smoke Transport Modeling, *J.
614 Appl. Meteorol. Climatol.*, 55, 3-22, doi: <http://dx.doi.org/10.1175/JAMC-D-15-0083.1>, 2016.
- 615 Chapman, E. G., Gustafson Jr., W. I., Easter, R. C., Barnard, J. C., Ghan, S. J., Pekour, M. S., and
616 Fast, J. D.: Coupling aerosolcloud-radiative processes in the WRF-Chem model: Investigating
617 the radiative impact of elevated point sources, *Atmos. Chem. Phys.*, 9, 945–964,
618 doi:10.5194/acp-9-945-2009, 2009.

- 619 Chen, D., Xie, X., Zhou, Y., Lang, J., Xu, T., Yang, N., Zhao, Y., and Liu, X.: Performance
620 Evaluation of the WRF-Chem Model with Different Physical Parameterization Schemes
621 during an Extremely High PM_{2.5} Pollution Episode in Beijing. *Aerosol and Air Quality*
622 *Research*, 17:262-277. doi: 10.4209/aaqr.2015.10.0610, 2017.
- 623 Chen, J., Lu, J., Avise, J. C., DaMassa, J. A., Kleeman, M. J., and Kaduwela, A. P.: Seasonal
624 modeling of PM_{2.5} in California's San Joaquin Valley, *Atmos. Environ.*, 92, 182–190, 2014.
- 625 Chew, B. N., J. R. Campbell, J. S. Reid, D. M. Giles, E. J. Welton, S. V. Salinas and S. C. Liew :
626 Tropical cirrus cloud contamination in sun photometer data, *Atmos. Env.*, 45, 6724-6731,
627 doi:10.1016/j.atmosenv.2011.08.017, 2011.
- 628 Chow, J. C., Chen, L. W. A., Watson, J. G., Lowenthal, D. H., Magliano, K. A., Turkiewicz, K.,
629 Lehrman, D. E.: PM_{2.5} chemical composition and spatiotemporal variability during the
630 California regional PM₁₀/PM_{2.5} air quality study (CRPAQS), *J. Geophys. Res.-Atmos.*, 111,
631 D10S04, doi:10.1029/2005JD006457, 2006.
- 632 Cuchiara, G.C., Li, X., Carvalho, J., and Rappenglück, B.: Intercomparison of planetary boundary
633 layer parameterization and its impacts on surface ozone concentration in the WRF/Chem
634 model for a case study in Houston/Texas. *Atmospheric Environment*, 96,175–185.
635 <http://dx.doi.org/10.1016/j.atmosenv.2014.07.013>, 2014.
- 636 Dee, D. P., Uppala, S. M., Simmons, A. J., Berrisford, P., Poli, P, Kobayashi, S., Andrae, U.,
637 Balmaseda, M. A., Balsamo, G., Bauer, P., Bechtold, P., Beljaars, A. C. M., van de Berg, L.,
638 Bidlot, J., Bormann, N., Delsol, C., Dragani, R., Fuentes, M., Geer, A. J., Haimberger, L.,
639 Healy, S. B., Hersbach, H., Hólm, E. V., Isaksen, L., Kallberg, P., Köhler, M., Matricardi, M.,
640 McNally, A. P., Monge-Sanz, B. M., Morcrette, J.-J., Park, B.-K., Peubey, C., de Rosnay, P.,
641 Tavolato, C., Thépaut, J.-N., and Vitart, F.: The ERA-Interim reanalysis: configuration and
642 performance of the data assimilation system, *Q. J. R. Meteorol. Soc.*, 137, 553–597, 2011.
- 643 Diner, D. J., Beckert, J. C., Reilly, T. H., Bruegge, C. J., Conel, J. E., Kahn, R. A., Martonchik, J.
644 V., Ackerman, T. P., Davies, R., Gerstl, S. A. W., Gordon, H. R., Muller, J. P., Myneni, R. B.,
645 Sellers, P. J., Pinty, B., and Verstraete, M. M.: Multi-angle Imaging SpectroRadiometer
646 (MISR) Instrument Description and Experiment Overview, *IEEE T. Geosci. Remote*, 36,
647 1072–1087, 1998.

- 648 Divakarla, M. G., Barnet, C. D., Goldberg, M. D., McMillin, L. M., Maddy, E., Wolf, W., Zhou,
649 L., and Liu, X.: Validation of Atmospheric Infrared Sounder temperature and water vapor
650 retrievals with matched radiosonde measurements and forecasts, *J. Geophys. Res.*, 111,
651 D09S15, doi:10.1029/2005JD006116, 2006.
- 652 Eck, T. F., Holben, B. N., Reid, J. S., Dubovik, O., Smirnov, A., O'Neill, N. T., Slutsker, I., and
653 Kinn, S.: Wavelength dependence of the optical depth of biomass burning urban, and desert
654 dust aerosols, *J. Geophys. Res.*, 104, 31333–31349, 1999.
- 655 Emmons, L. K., Walters, S., Hess, P. G., Lamarque, J.-F., Pfister, G. G., Fillmore, D., Granier, C.,
656 Guenther, A., Kinnison, D., Laepple, T., Orlando, J., Tie, X., Tyndall, G., Wiedinmyer, C.,
657 Baughcum, S. L., and Kloster, S.: Description and evaluation of the Model for Ozone and
658 Related chemical Tracers, version 4 (MOZART-4), *Geosci. Model Dev.*, 3, 43–67, doi:
659 10.5194/gmd-3-43-2010, 2010.
- 660 Fast, J. D., Gustafson Jr., W. I., Easter, R. C., Zaveri, R. A., Barnard, J. C., Chapman, E. G., Grell,
661 G. A. and Peckham, S. E.: Evolution of ozone, particulates, and aerosol direct radiative forcing
662 in the vicinity of Houston using a fully coupled meteorology-chemistry-aerosol model, *J.*
663 *Geophys. Res.*, 111, D21305, doi:10.1029/2005JD006721, 2006.
- 664 Fast, J. D., Gustafson Jr., W. I., Berg, L. K., Shaw, W. J., Pekour, M., Shrivastava, M., Barnard, J.
665 C., Ferrare, R. A., Hostetler, C. A., Hair, J. A., Erickson, M., Jobson, B. T., Flowers, B., Dubey,
666 M. K., Springston, S., Pierce, R. B., Dolislager, L., Pederson, J., and Zaveri, R. A.: Transport
667 and mixing patterns over Central California during the carbonaceous aerosol and radiative
668 effects study (CARES), *Atmos. Chem. Phys.*, 12, 1759-1783, doi:10.5194/acp-12-1759-2012,
669 2012.
- 670 Fast, J. D., Allan, J., Bahreini, R., Craven, J., Emmons, L., Ferrare, R., Hayes, P. L., Hodzic, A.,
671 Holloway, J., Hostetler, C., Jimenez, J. L., Jonsson, H., Liu, S., Liu, Y., Metcalf, A.,
672 Middlebrook, A., Nowak, J., Pekour, M., Perring, A., Russell, L., Sedlacek, A., Seinfeld, J.,
673 Setyan, A., Shilling, J., Shrivastava, M., Springston, S., Song, C., Subramanian, R., Taylor, J.
674 W., Vinoj, V., Yang, Q., Zaveri, R. A., and Zhang, Q.: Modeling regional aerosol and aerosol
675 precursor variability over California and its sensitivity to emissions and long-range transport
676 during the 2010 CalNex and CARES campaigns, *Atmos. Chem. Phys.*, 14, 10013-10060,
677 doi:10.5194/acp-14-10013-2014, 2014.

- 678 Feingold, G., and Morley, B.: Aerosol hygroscopic properties as measured by lidar and comparison
679 with in situ measurements, *J. Geophys. Res.*, 108(D11), 4327, doi:10.1029/2002JD002842,
680 2003.
- 681 Flanner, M. G., and Zender, C. S.: Snowpack radiative heating: Influence on Tibetan Plateau
682 climate, *Geophys. Res. Lett.*, 32, L06501, doi:10.1029/2004GL022076, 2005.
- 683 Flanner, M. G., and Zender, C. S.: Linking snowpack microphysics and albedo evolution, *J.*
684 *Geophys. Res.*, 111, D12208, doi:10.1029/2005JD006834, 2006.
- 685 Fountoukis, C., Koraj, D., Denier van der Gon, H. A. C., Charalampidis, P. E., Pilinis, C., and
686 Pandis, S. N.: Impact of grid resolution on the predicted fine PM by a regional 3-D chemical
687 transport model, *Atmos. Environ.*, 68, 24–32, 2013.
- 688 Freitas, S. R., Longo, K. M., Alonso, M. F., Pirre, M., Marecal, V., Grell, G., Stockler, R., Mello,
689 R. F., and Sánchez Gácita, M.: PREP-CHEM-SRC – 1.0: a preprocessor of trace gas and
690 aerosol emission fields for regional and global atmospheric chemistry models, *Geosci. Model*
691 *Dev.*, 4, 419-433, doi:10.5194/gmd-4-419-2011, 2011.
- 692 Ghan, S., Laulainen, N., Easter, R., Wagener, R., Nemesure, S., Chapman, E., Zhang, Y., and
693 Leung, R.: Evaluation of aerosol direct radiative forcing in MIRAGE, *J. Geophys. Res.*,
694 106(D6), 5295–5316, doi:10.1029/2000JD900502, 2001.
- 695 Ginoux, P., Chin, M., Tegen, I., Prospero, J. M., Holben, B., Dubovik, O., and Lin, S.: Sources
696 and distributions of dust aerosols simulated with the GOCART model, *J. Geophys. Res.*, 106,
697 20225–20273, 2001.
- 698 Gong, S. L.: A parameterization of sea-salt aerosol source function for sub- and super-micron
699 particles, *Global Biogeochem. Cy.*, 17, 1097, doi:10.1029/2003GB002079, 2003.
- 700 Grell, G. and Devenyi, D.: A generalized approach to parameterizing convection combining
701 ensemble and data assimilation techniques, *Geophys. Res. Lett.*, 29(14),
702 doi:10.1029/2002GL015311, 2002.
- 703 Grell, G., Peckham, S., Schmitz, R., et al.: Fully coupled “online” chemistry within the WRF
704 model, *Atmos. Environ.*, 39(37), 6957–6975, 2005.

- 705 Grell, G., Freitas, S. R., Stuefer, M., and Fast, J.: Inclusion of biomass burning in WRF-Chem:
706 impact of wildfires on weather forecasts, *Atmos. Chem. Phys.*, 11, 5289-5303,
707 doi:10.5194/acp-11-5289-2011, 2011.
- 708 Guenther, A., Karl, T., Harley, P., Wiedinmyer, C., Palmer, P. I., and Geron, C.: Estimates of
709 global terrestrial isoprene emissions using MEGAN (Model of Emissions of Gases and
710 Aerosols from Nature), *Atmos. Chem. Phys.*, 6, 3181–3210, doi: 10.5194/acp-6-3181-2006,
711 2006.
- 712 Hand, J., Copeland, S. A., Day, D. E., Dillner, A. M., Indresand, H., Malm, W. C., McDade, C.
713 E., Moore Jr., C. T., Pitchford, M. L., Schichtel, B. A., and Watson, J. G.: Spatial and seasonal
714 patterns and temporal variability of haze and its constituents in the United States: Report V,
715 June 2011, available at: [http://vista.cira.colostate.edu/Improve/spatial-and-seasonal-patterns-](http://vista.cira.colostate.edu/Improve/spatial-and-seasonal-patterns-and-temporal-variability-of-haze-and-its-constituents-in-the-united-states-report-v-june-2011/)
716 [and-temporal-variability-of-haze-and-its-constituents-in-the-united-states-report-v-june-](http://vista.cira.colostate.edu/Improve/spatial-and-seasonal-patterns-and-temporal-variability-of-haze-and-its-constituents-in-the-united-states-report-v-june-2011/)
717 [2011/](http://vista.cira.colostate.edu/Improve/spatial-and-seasonal-patterns-and-temporal-variability-of-haze-and-its-constituents-in-the-united-states-report-v-june-2011/), 2011.
- 718 Hasheminassab, S., Daher, N., Saffari, A., Wang, D., Ostro, B. D., and Sioutas, C.: Spatial and
719 temporal variability of sources of ambient fine particulate matter (PM_{2.5}) in California, *Atmos.*
720 *Chem. Phys.*, 14, 12085-12097, doi:10.5194/acp-14-12085-2014, 2014.
- 721 Herner, J. D., Ying, Q., Aw, J., Gao, O., Chang, D. P. Y., and Kleeman, M.: Dominant mechanisms
722 that shape the airborne particle size and composition in central California, *Aerosol Sci.*
723 *Technol.*, 40, 827–844, 2006.
- 724 Holben, B. N., Eck, T. F., Slutsker, I., Tanre, D., Buis, J. P., Setzer, A., Vermote, E., Reagan, J.
725 A., Kaufman, Y. J., Nakajima, T., Lavenu, F., Jankowiak, I., and Smirnov, A.: AERONET –
726 A Federated Instrument Network and Data Archive for Aerosol Characterization, *Remote*
727 *Sens. Environ.*, 66, 1–16, 1998.
- 728 Holben, B. N., Tanr, D., Smirnov, A., Eck, T. F., Slutsker, I., Abuhassan, N., Newcomb, W. W.,
729 Schafer, J. S., Chatenet, B., Lavenu, F., Kaufman, Y. J., Castle, J. V., Setzer, A., Markham,
730 B., Clark, D., Frouin, R., Halthore, R., Karneli, A., O'Neill, N. T., Pietras, C., Pinker, R. T.,
731 Voss, K., and Zibordi, G.: An emerging ground-based aerosol climatology: Aerosol optical
732 depth from AERONET, *J. Geophys. Res.*, 106, 12067–12097, 2001.

- 733 Hong, S., Noh, Y., and Dudhia, J.: A new vertical diffusion package with an explicit treatment of
734 entrainment processes, *Mon. Weather Rev.*, 134, 2318–2341, 2006.
- 735 Hu, X. M., Nielsen-Gammon, J.W., and Zhang, F.: Evaluation of three planetary boundary layer
736 schemes in the WRF model, *J. Appl. Meteorol. Climatol.*, 49(9), 1831–1844,
737 doi:10.1175/2010JAMC2432.1, 2010.
- 738 Hu, Z., Zhao, C., Huang, J., Leung, L. R., Qian, Y., Yu, H., Huang, L., and Kalashnikova, O. V.:
739 Trans-Pacific transport and evolution of aerosols: evaluation of quasi-global WRF-Chem
740 simulation with multiple observations, *Geosci. Model Dev.*, 9, 1725–1746, doi:10.5194/gmd-
741 9-1725-2016, 2016.
- 742 Iacono, M. J., Delamere, J. S., Mlawer, E. J., Shephard, M. W., Clough, S. A., and Collins, W. D.:
743 Radiative forcing by long-lived greenhouse gases: calculations with the AER radiative transfer
744 models, *J. Geophys. Res.*, 113, D13103, doi:10.1029/2008JD009944, 2008.
- 745 Jaeglé, L., Quinn, P. K., Bates, T. S., Alexander, B., and Lin, J.-T.: Global distribution of sea salt
746 aerosols: new constraints from in situ and remote sensing observations, *Atmos. Chem. Phys.*,
747 11, 3137–3157, doi:10.5194/acp-11-3137-2011, 2011.
- 748 Kahn, R. A., Gaitley, B. J., Garay, M. J., Diner, D. J., Eck, T. F., Smirnov, A., and Holben, B. N.:
749 Multiangle Imaging SpectroRadiometer global aerosol product assessment by comparison with
750 the Aerosol Robotic Network, *J. Geophys. Res.*, 115, D23209, doi:10.1029/2010JD014601,
751 2010.
- 752 Kassianov, E., Pekour, M., and Barnard, J.: Aerosols in central California: Unexpectedly large
753 contribution of coarse mode to aerosol radiative forcing, *Geophys. Res. Lett.*, 39, L20806, doi:
754 10.1029/2012GL053469, 2012.
- 755 Kelly, J. T., Baker, K. R., Nowak, J. B., Murphy, J. G., Markovic, M. Z., VandenBoer, T. C., Ellis,
756 R. A., Neuman, J. A., Weber, R. J., and Roberts, J. M.: Fine-scale simulation of ammonium
757 and nitrate over the South Coast Air Basin and San Joaquin Valley of California during
758 CalNex-2010, *J. Geophys. Res.-Atmos.*, 119, 3600–3614, 2014.
- 759 Lawrence, D. M., Oleson, K. W., Flanner, M. G., Thornton, P. E., Swenson, S. C., Lawrence, P.
760 J., Zeng, X., Yang, Z.-L., Levis, S., Sakaguchi, K., Bonan, G. B., and Slater, A. G.:
761 Parameterization improvements and functional and structural advances in version 4 of the

- 762 Community Land Model, *J. Adv. Model. Earth Sys.*, 3, M03001, doi:
763 10.1029/2011MS000045, 2011.
- 764 Misemis, C. and Zhang, Y.: An examination of sensitivity of WRF/Chem predictions to physical
765 parameterizations, horizontal grid spacing, and nesting options, *Atmos. Res.*, 97, 315–334,
766 doi:10.1016/j.atmosres.2010.04.005, 2010.
- 767 Morabito, D., Wu, L., and Slobin, S.: Weather Forecasting for Ka-band Operations: Initial Study
768 Results, IPN PR 42-206, pp. 1-24, August 15, 2016. Available at:
769 http://ipnpr.jpl.nasa.gov/progress_report/42-206/206C.pdf, 2016.
- 770 Morrison, H., Thompson, G., and Tatarskii, V.: Impact of cloud microphysics on the development
771 of trailing stratiform precipitation in a simulated squall line: comparison of one- and two-
772 moment schemes, *Mon. Weather Rev.*, 137, 991–1007, 2009.
- 773 Omar, A.H., Winker, D.M., Kittaka, C., Vaughan, M.A., Liu, Z., Hu, Y., Trepte, C.R., Rogers,
774 R.R., Ferrare, R.A., Lee, K.P., Kuehn, R.E., Hostetler, C.A.: The CALIPSO automated aerosol
775 classification and lidar ratio selection algorithm. *J. Atmos. Ocean. Technol.* 26, 1994–2014,
776 2009.
- 777 Pleim, J. E.: A combined local and nonlocal closure model for the atmospheric boundary layer.
778 Part I: Model description and testing, *J. Appl. Meteorol. Clim.*, 46, 1383–1395, 2007.
- 779 Pun, B. K., Balmori, R. T. F., and Seigneur, C.: Modeling wintertime particulate matter formation
780 in central California, *Atmos. Environ.*, 43, 402–409, 2009.
- 781 Qian, Y., Gustafson Jr., W. I., and Fast, J. D.: An investigation of the sub-grid variability of trace
782 gases and aerosols for global climate modeling, *Atmos. Chem. Phys.*, 10, 6917–6946,
783 doi:10.5194/acp-10-6917-2010, 2010.
- 784 Randerson, J. T., van der Werf, G. R., Giglio, L., Collatz, G. J., and Kasibhatla, P. S.: Global Fire
785 Emissions Database, Version 2 (GFEDv2.1). Data set. Available on-line [<http://daac.ornl.gov/>]
786 from Oak Ridge National Laboratory Distributed Active Archive Center, Oak Ridge,
787 Tennessee, U.S.A. doi:10.3334/ORNLDAAC/849, 2007.
- 788 San Joaquin Valley Air Pollution Control District: 2012 PM_{2.5} plan. Available from:
789 http://www.valleyair.org/Air_Quality_Plans/PM25Plans2012.htm, 2012.

- 790 Scarino, A. J., Obland, M. D., Fast, J. D., Burton, S. P., Ferrare, R. A., Hostetler, C. A., Berg, L.
791 K., Lefer, B., Haman, C., Hair, J. W., Rogers, R. R., Butler, C., Cook, A. L., and Harper, D.
792 B.: Comparison of mixed layer heights from airborne high spectral resolution lidar, ground-
793 based measurements, and the WRF-Chem model during CalNex and CARES, *Atmos. Chem.*
794 *Phys.*, 14, 5547-5560, doi:10.5194/acp-14-5547-2014, 2014.
- 795 Shaw, W., Allwine, K. J., Fritz, B. G., Rutz, F. C., Rishel, J. P., and Chapman, E. G.: An evaluation
796 of the wind erosion module in DUSTRAN, *Atmos. Environ.*, 42, 1907–1921, 2008.
- 797 Solomon, P. A., Crumpler, D., Flanagan, J. B., Jayanty, R. K. M., Rickman, E. E., and McDade C.
798 E.: U.S. National PM_{2.5} Chemical Speciation Monitoring Networks – CSN and IMPROVE:
799 Description of Networks, *J. Air Waste Manage.*, 64, 1410–1438,
800 doi:10.1080/10962247.2014.956904, 2014.
- 801 Susskind, J., Barnet, C. D., and Blaisdell, J.: Retrieval of atmospheric and surface parameters from
802 AIRS/AMSU/HSB data under cloudy conditions, *IEEE Trans. Geosci. Remote Sens.*, 41(2),
803 390–409, doi:10.1109/TGRS.2002.808236, 2003.
- 804 Schuster, G. L., Dubovik, O., and Holben, B. N.: Angström exponent and bimodal aerosol size
805 distributions, *J. Geophys. Res.*, 111, D07207, doi:10.1029/2005JD006328, 2006.
- 806 Tessum, C. W., Hill, J. D., and Marshall, J. D.: Twelve-month, 12 km resolution North American
807 WRF-Chem v3.4 air quality simulation: performance evaluation, *Geosci. Model Dev.*, 8, 957-
808 973, doi:10.5194/gmd-8-957-2015, 2015.
- 809 Toth, T. D., Campbell, J. R., Reid, J. S., Tackett, J. L., Vaughan, M. A. and Zhang, J.: Lower
810 daytime threshold sensitivities to aerosol optical thickness in CALIPSO Level 2 products, *J.*
811 *Geophys. Res.*, in review, 2017.
- 812 US Environmental Protection Agency, 2010: Technical Support Document: Preparation of
813 Emissions Inventories for the Version 4, 2005-based Platform, 73 pp., Office of Air Quality
814 Planning and Standards, Air Quality Assessment Division, available at:
815 https://www3.epa.gov/crossstaterule/pdfs/2005_emissions_tsd_07jul2010.pdf, 2010.
- 816 Wu, L., and Petty, G. W. : Intercomparison of Bulk Microphysics Schemes in Simulations of Polar
817 lows. *Mon. Wea. Rev.*, 138, 2211-2228. doi: 10.1175/2010MWR3122.1, 2010.

- 818 Wu, L., Su, H. and Jiang, J. H.: Regional simulations of deep convection and biomass burning
819 over South America: 1. Model evaluations using multiple satellite data sets, *J. Geophys. Res.*,
820 116, D17208, doi:10.1029/2011JD016105, 2011a.
- 821 Wu, L., Su, H. and Jiang, J. H.: Regional simulations of deep convection and biomass burning
822 over South America: 2. Biomass burning aerosol effects on clouds and precipitation, *J.*
823 *Geophys. Res.*, 116, D17209, doi:10.1029/2011JD016106, 2011b.
- 824 Wu, L., Su, H. and Jiang, J. H.: Regional simulations of aerosol impacts on precipitation during
825 the East Asian summer monsoon. *J. Geophys. Res. Atmos.*, 118, doi: 10.1002/jgrd.50527,
826 2013.
- 827 Wu, L., Li, J.-L. F., Pi, C.-J., Yu, J.-Y., and Chen, J.-P.: An observationally based evaluation of
828 WRF seasonal simulations over the Central and Eastern Pacific, *J. Geophys. Res. Atmos.*, 120,
829 doi:10.1002/2015JD023561, 2015.
- 830 Xie, B., Fung, J. C. H., Chan, A., and Lau, A.: Evaluation of nonlocal and local planetary boundary
831 layer schemes in the WRF model, *J. Geophys. Res.*, 117, D12103, doi:10.1029/2011JD017080,
832 2012.
- 833 Ying, Q. and Kleeman, M. J.: Regional contributions to airborne particulate matter in central
834 California during a severe pollution episode, *Atmos. Environ.*, 43, 1218–1228, 2009.
- 835 Young, S.A. and Vaughan, M.A.: The retrieval of profiles of particulate extinction from Cloud–
836 Aerosol Lidar Infrared Pathfinder Satellite Observations (CALIPSO) data: algorithm
837 description. *J. Atmos. Ocean. Technol.* 26, 1105–1119, 2009.
- 838 Zaveri, R. A. and Peters, L. K.: A new lumped structure photochemical mechanism for large-scale
839 applications, *J. Geophys. Res.*, 104, 30387–30415, 1999.
- 840 Zaveri, R. A., Easter, R. C., Fast, J. D., and Peters, L. K.: Model for Simulating Aerosol
841 Interactions and Chemistry (MOSAIC), *J. Geophys. Res.*, 113, D13204,
842 doi:10.1029/2007JD008782, 2008.
- 843 Zhang, Y., Liu, P., Liu, X.-H., Pun, B., Seigneur, C., Jacobson, M. Z., and Wang, W.-X.: Fine
844 scale modeling of wintertime aerosol mass, number, and size distributions in central California,
845 *J. Geophys. Res.-Atmos.*, 115, D15207, doi:10.1029/2009jd012950, 2010.

- 846 Zhao, C., Liu, X., Leung, L. R., Johnson, B., McFarlane, S. A., Gustafson Jr., W. I., Fast, J. D.,
847 and Easter, R.: The spatial distribution of mineral dust and its shortwave radiative forcing over
848 North Africa: modeling sensitivities to dust emissions and aerosol size treatments, *Atmos.*
849 *Chem. Phys.*, 10, 8821–8838, doi: 10.5194/acp-10-8821-2010, 2010.
- 850 Zhao, C., Liu, X., Ruby Leung, L., and Hagos, S.: Radiative impact of mineral dust on monsoon
851 precipitation variability over West Africa, *Atmos. Chem. Phys.*, 11, 1879–1893,
852 doi:10.5194/acp-11-1879-2011, 2011.
- 853 Zhao, C., Chen, S., Leung, L. R., Qian, Y., Kok, J. F., Zaveri, R. A., and Huang, J.: Uncertainty in
854 modeling dust mass balance and radiative forcing from size parameterization, *Atmos. Chem.*
855 *Phys.*, 13, 10733-10753, doi:10.5194/acp-13-10733-2013, 2013a.
- 856 Zhao, C., Leung, L. R., Easter, R., Hand, J., and Avise, J.: Characterization of speciated aerosol
857 direct radiative forcing over California, *J. Geophys. Res.*, 118, 2372–2388, doi:
858 10.1029/2012JD018364, 2013b.
- 859 Zhao, C., Hu, Z., Qian, Y., Ruby Leung, L., Huang, J., Huang, M., Jin, J., Flanner, M. G., Zhang,
860 R., Wang, H., Yan, H., Lu, Z., and Streets, D. G.: Simulating black carbon and dust and their
861 radiative forcing in seasonal snow: a case study over North China with field campaign
862 measurements, *Atmos. Chem. Phys.*, 14, 11475-11491, doi:10.5194/acp-14-11475-2014,
863 2014.

864 **List of Table**

865 Table 1. Experiment description

Experiment ID	Experiment description
20km	Simulation with the GOCART dust scheme at 20 km horizontal resolution.
20km_D2	Same as 20km, but with the DUSTRAN dust scheme.
20km_P7	Same as 20km_D2, but with the ACM2 PBL scheme.
4km	Same as 20km, but at 4 km horizontal resolution.
4km_D2	Same as 4km, but with the DUSTRAN dust scheme.

866

867 Table 2. Correlation with observations for different species at Fresno, CA

Species	20km	4km	4km_D2	20km_D2	20km_P7
PM _{2.5}	0.89	0.90	0.86	0.78	0.03
PM _{2.5} _NO ₃	0.94	0.95	0.94	0.94	0.91
PM _{2.5} _NH ₄	0.97	0.96	0.96	0.98	0.96
PM _{2.5} _OM	0.93	0.93	0.94	0.93	0.91
PM _{2.5} _EC	0.98	0.98	0.98	0.98	0.96
PM _{2.5} _SO ₄	0.63	-0.16	-0.14	0.61	0.63
PM _{2.5} _dust	-0.55	-0.50	0.48	0.55	0.36
PM ₁₀	-0.25	-0.23	-0.08	0.01	-0.03

868

869 Table 3. Surface aerosol mass ($\mu\text{g m}^{-3}$) for different species at Fresno, CA

Species	Cold season						Warm season					
	OBS	20km	4km	4km_ D2	20km_ _D2	20km_ _P7	OBS	20km	4km	4km_ D2	20km_ _D2	20km_ _P7
PM _{2.5}	16.84	13.71	21.38	22.48	14.90	13.77	8.44	4.91	6.29	12.85	10.12	14.85
PM _{2.5} _NO ₃	5.43	6.36	9.54	9.22	6.22	3.16	0.84	0.55	0.69	0.79	0.66	0.57
PM _{2.5} _NH ₄	1.42	1.97	2.99	2.88	1.91	0.98	0.40	0.19	0.24	0.20	0.16	0.13
PM _{2.5} _OM	5.39	0.92	2.07	2.07	0.93	1.04	2.47	0.49	0.87	0.87	0.50	0.55
PM _{2.5} _EC	1.08	0.52	1.12	1.13	0.52	0.58	0.32	0.27	0.49	0.49	0.27	0.30
PM _{2.5} _SO ₄	0.87	0.53	0.82	0.81	0.53	0.46	1.04	0.54	0.61	0.60	0.53	0.49
PM _{2.5} _dust	0.90	0.11	0.11	1.65	1.50	4.18	2.08	0.04	0.03	6.49	5.16	10.05
PM ₁₀	31.55	14.93	22.81	28.32	20.10	24.52	34.82	7.08	8.69	38.12	30.19	48.02

870

871 Supplementary Table 1. Correlation with surface observations for meteorological variables at
872 Fresno, CA

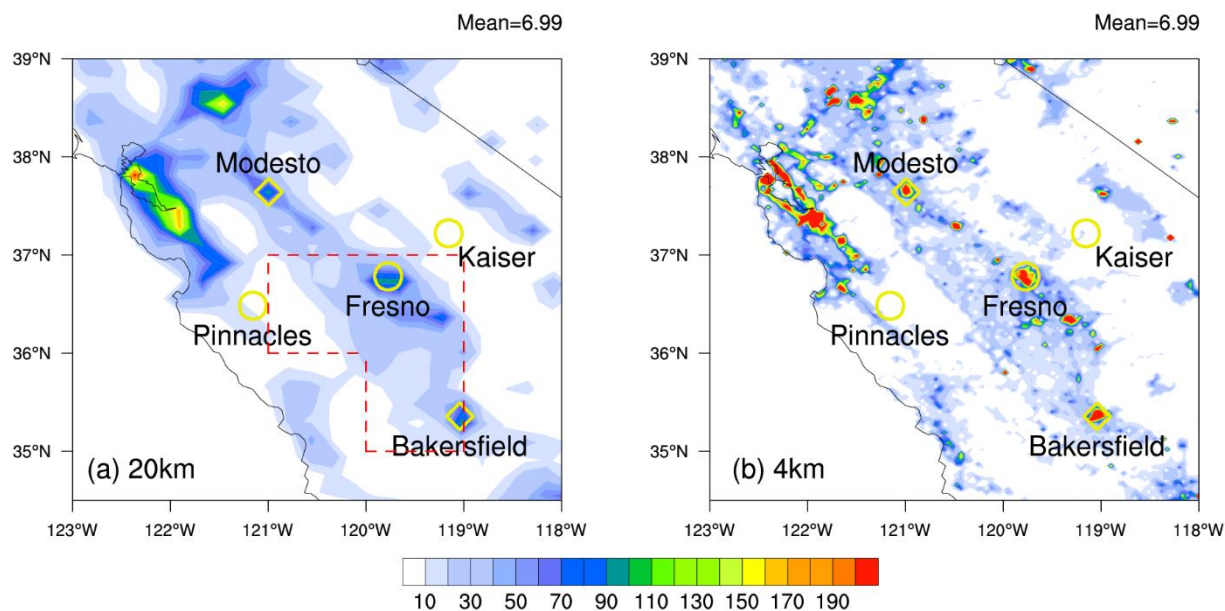
	4km_D2	20km_D2	20km_P7
T	0.94	0.94	0.94
RH	0.98	0.98	0.96
Wind	0.83	0.84	0.85
Rain	0.97	0.97	0.97

873

874 Supplementary Table 2. Bias for surface meteorological variables at Fresno, CA

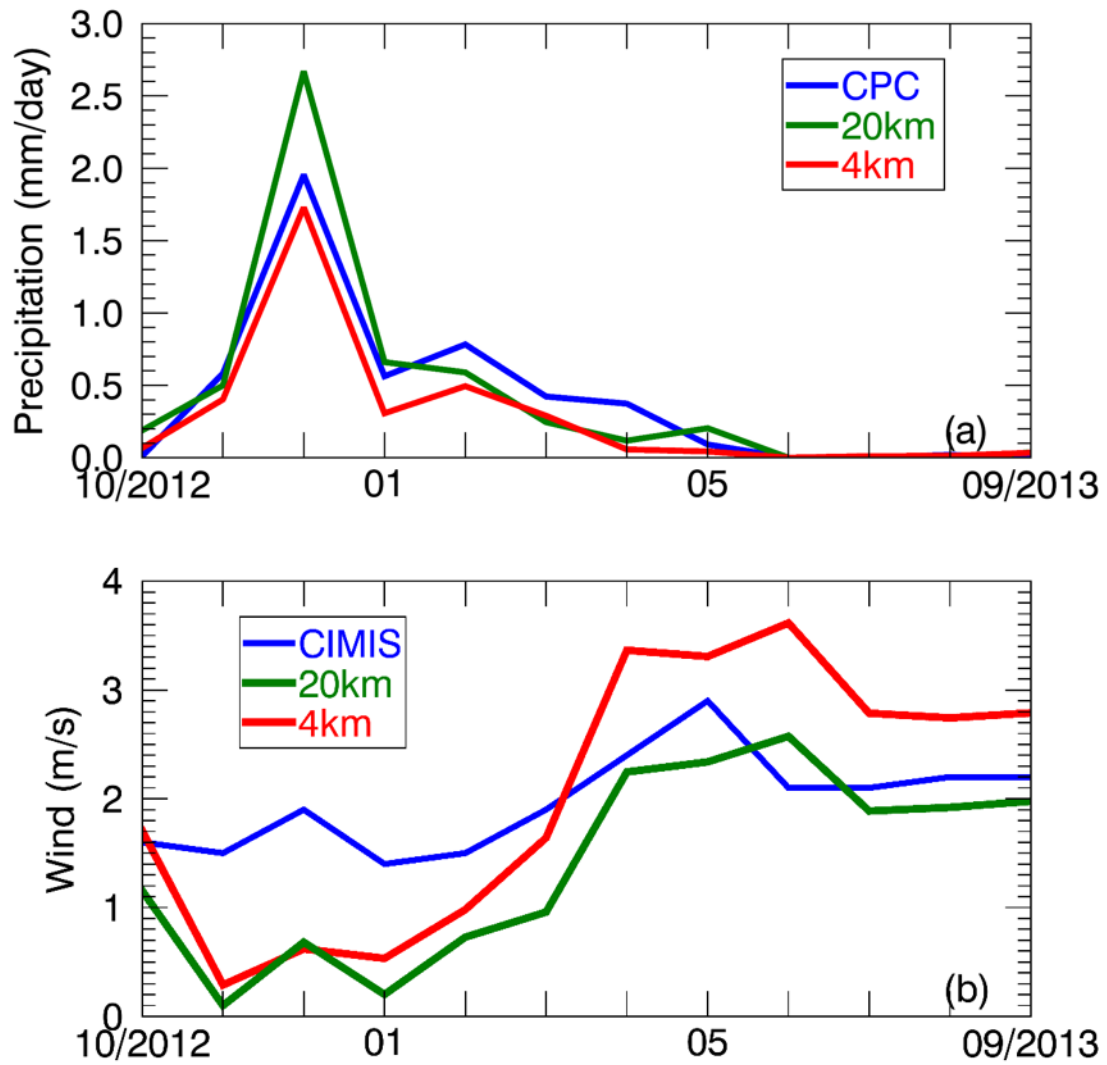
	Cold season			Warm season		
	4km_D2	20km_D2	20km_P7	4km_D2	20km_D2	20km_P7
T (K)	3.89	3.56	3.69	2.44	1.50	1.35
RH (%)	-9.78	-14.55	-19.35	-9.48	-9.32	-11.16
Wind (m/s)	-0.67	-1.00	-1.05	0.78	-0.16	-0.49
Rain (mm/day)	-0.15	0.14	-0.03	-0.06	-0.03	-0.04

875

876 **List of Figures**

877

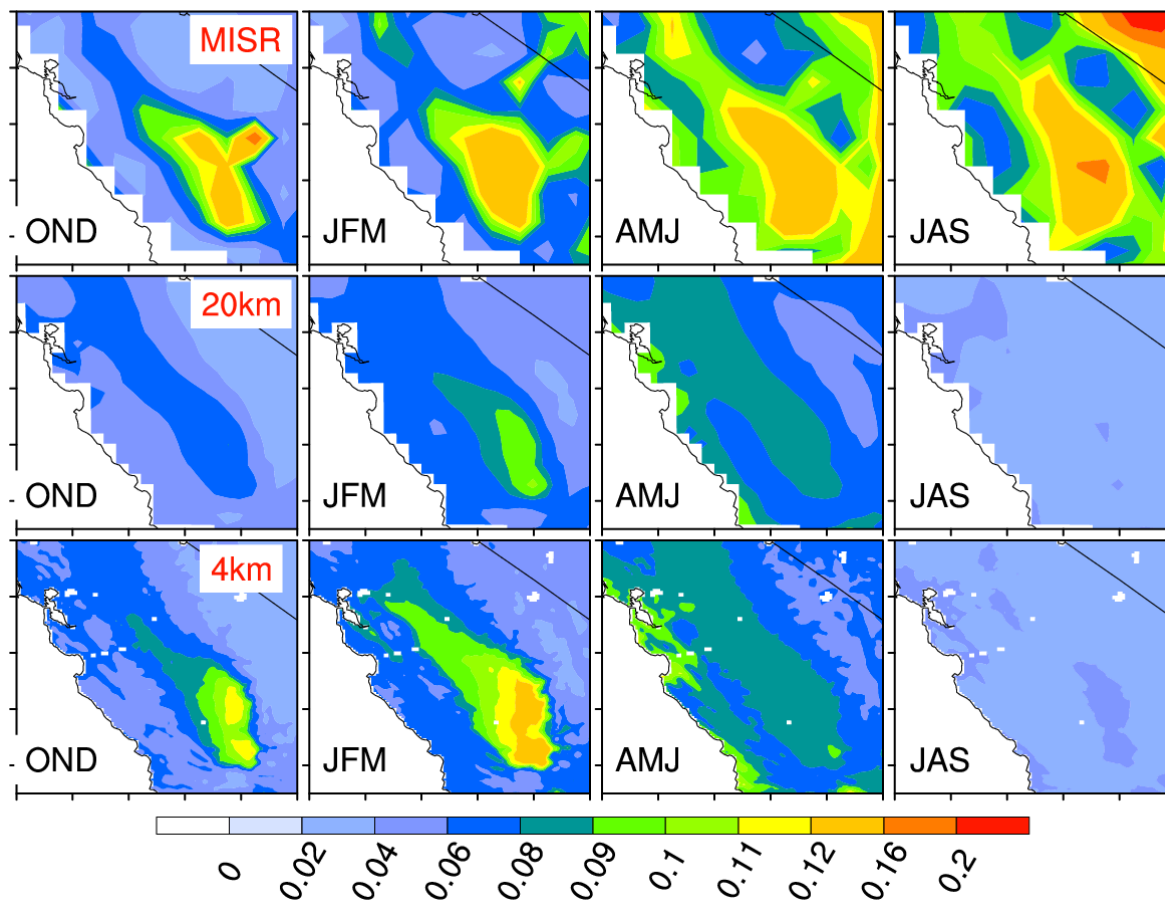
878 Figure 1. Daily mean anthropogenic $PM_{2.5}$ emission rate ($\mu\text{g m}^{-2} \text{hr}^{-1}$) at (a) 20km and (b) 4km
 879 simulation. Domain-averaged emission rate is shown at right corner of each figure. Red dashed
 880 lines in Figure 1a represent the region used for the domain averages in the discussions. Yellow
 881 circle: IMPROVE site; yellow diamond: EPA CSN site. Three urban sites: Fresno, Bakersfield and
 882 Modesto; two rural sites: Pinnacles and Kaiser.



883

884 Figure 2. (a) Monthly precipitation (mm/day) from CPC, 20km and 4km; (b) monthly wind speed

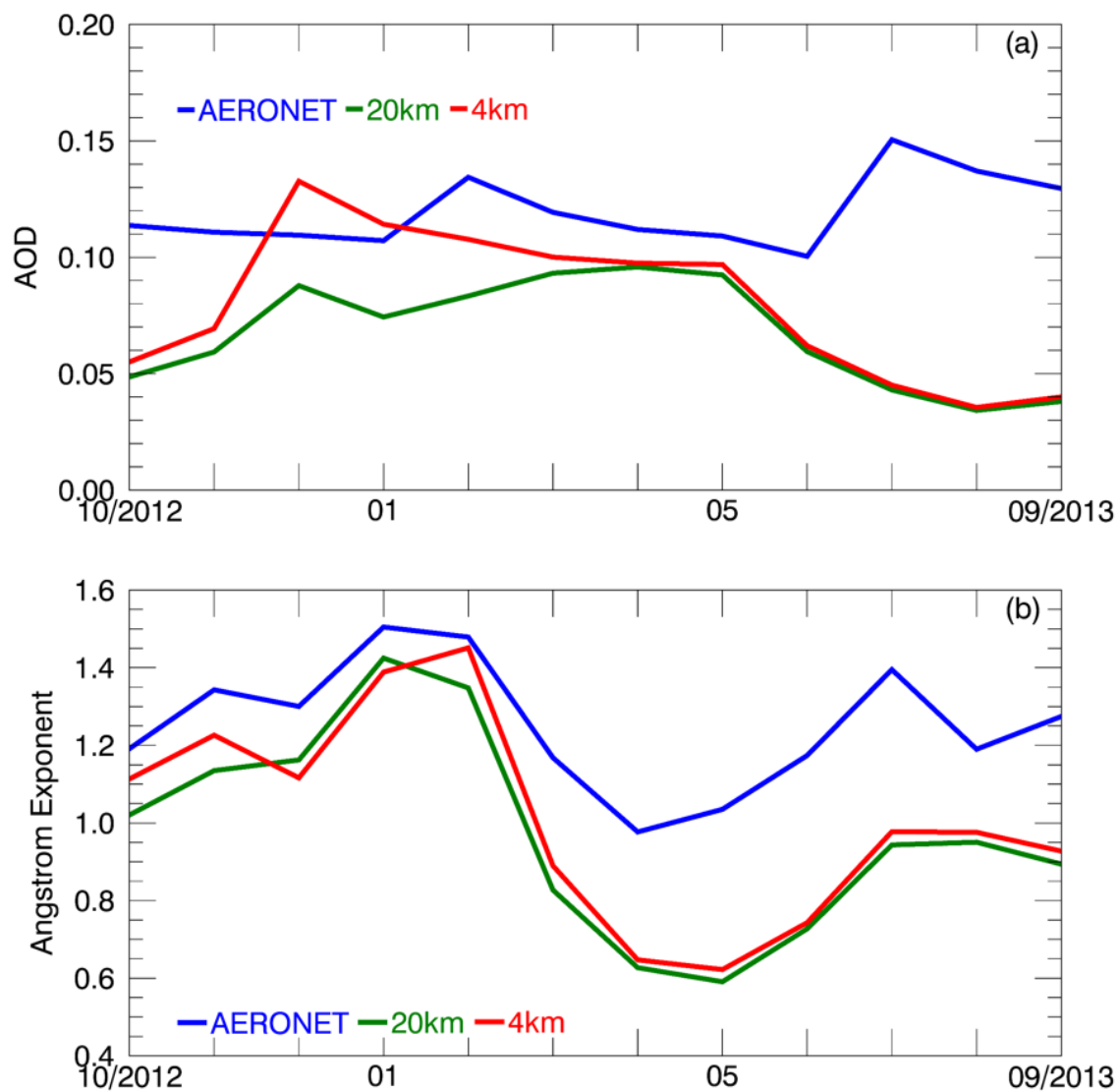
885 (m/s) from CIMIS, 20km and 4km. 4km_D2 (not shown) is similar to 4km.



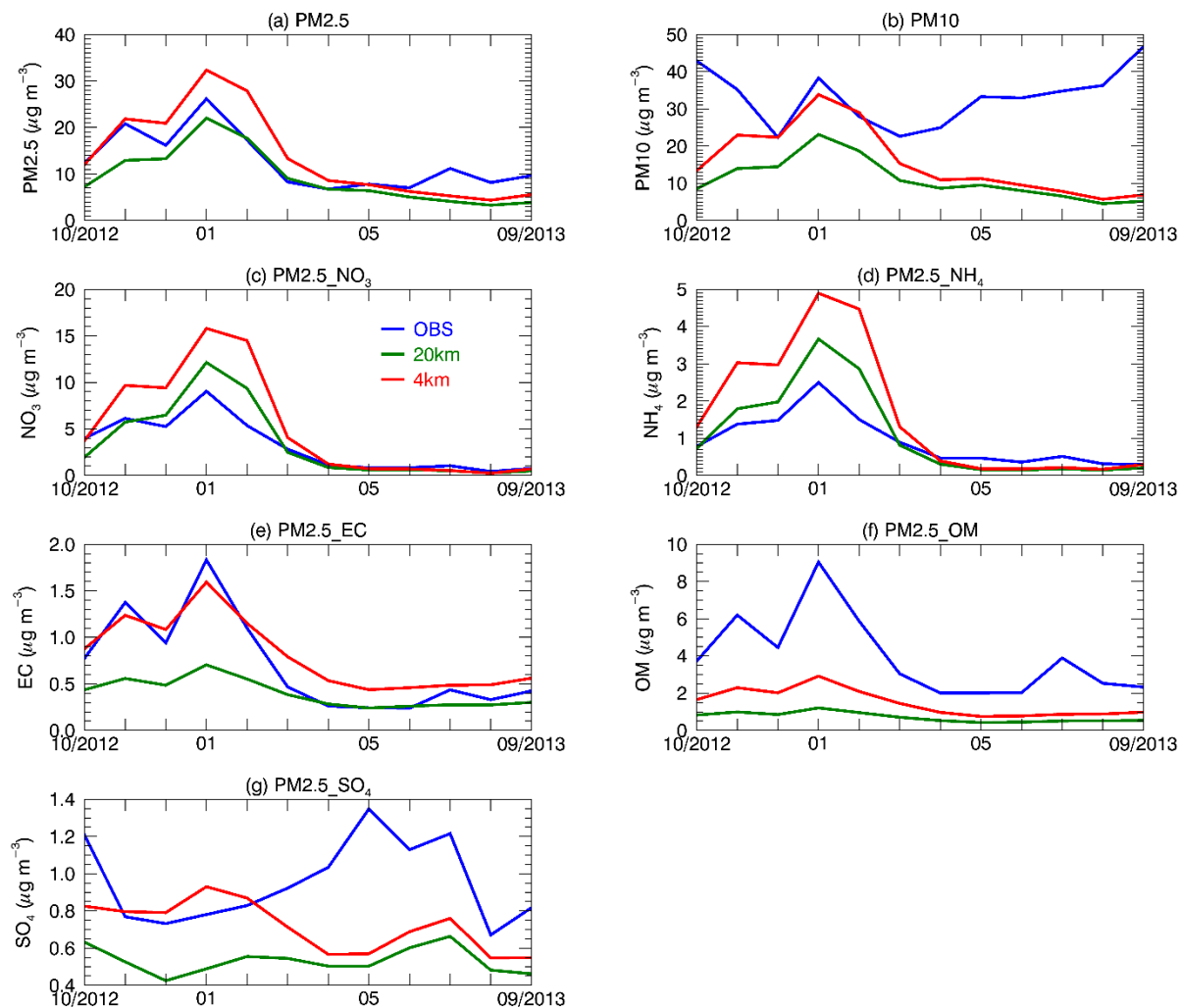
886

887 Figure 3. Spatial distribution of seasonal mean 550 nm AOD from MISR and the WRF-Chem
888 (20km and 4km) simulations in WY2013. OND: October-November-December; JFM: January-
889 February-March; AMJ: April-May-June; JAS: July-August-September.

890

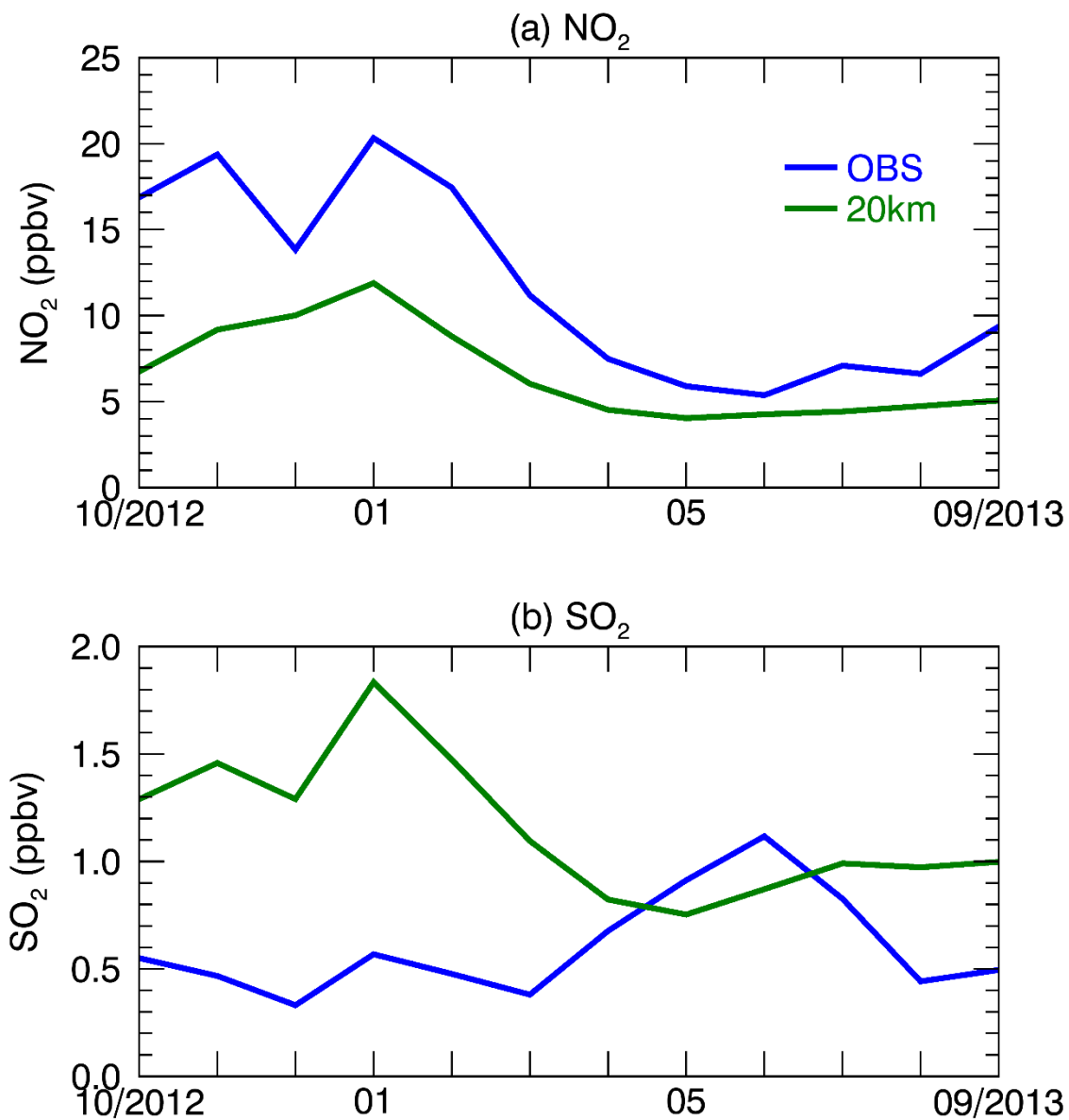


891
892 Figure 4. (a) Monthly mean 550 nm AOD; (b) monthly mean 400-600 nm Ångström exponent at
893 Fresno, CA from October 2012 to September 2013.



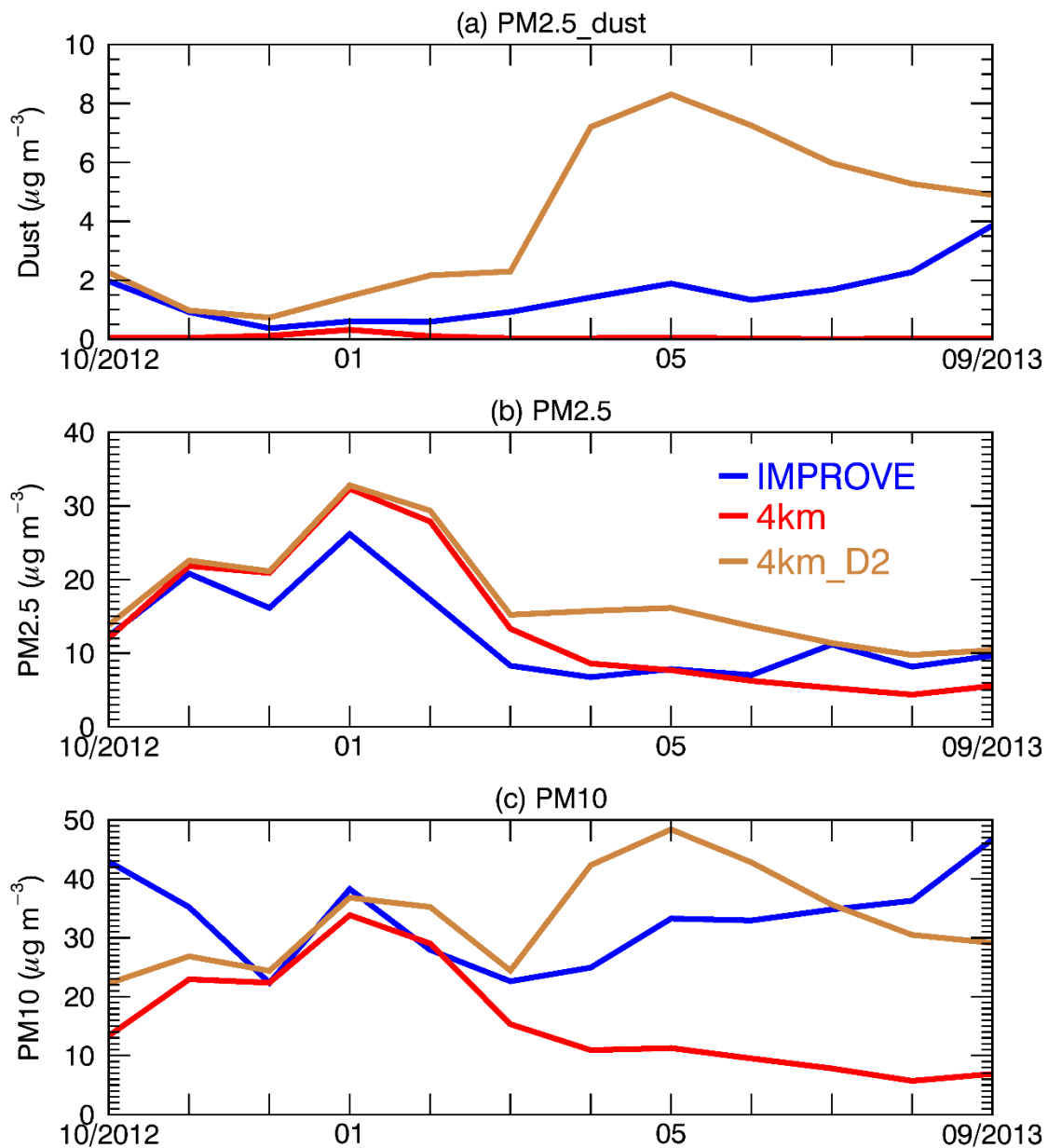
894

895 Figure 5. Aerosol mass ($\mu\text{g m}^{-3}$) for different species from OBS, the 20km and 4km simulations at
 896 Fresno, CA. NH_4 observations are from EPA; other observations are from IMPROVE. $\text{PM}_{2.5_}\text{NO}_3$
 897 represents NO_3 with diameter $\leq 2.5 \mu\text{m}$. Similar definition for NH_4 , EC, OM and SO_4 in the figures.

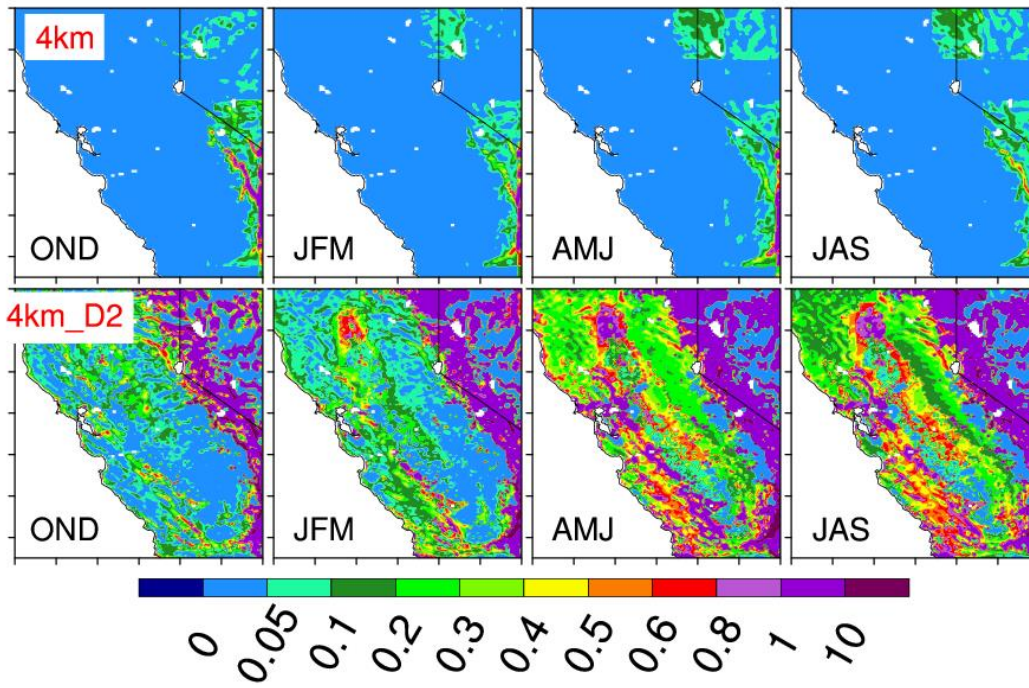


898

899 Figure 6. (a) NO_2 and (b) SO_2 from EPA (OBS) and the 20km run at Fresno, CA.

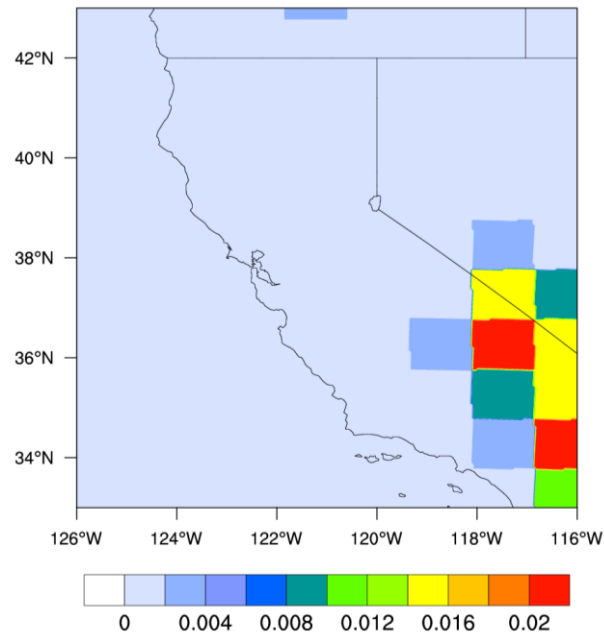


900
 901 Figure 7. (a) PM_{2.5_dust}; (b) PM_{2.5}; and (c) PM₁₀ from IMPROVE, the 4km and 4km_D2
 902 simulations at Fresno, CA.



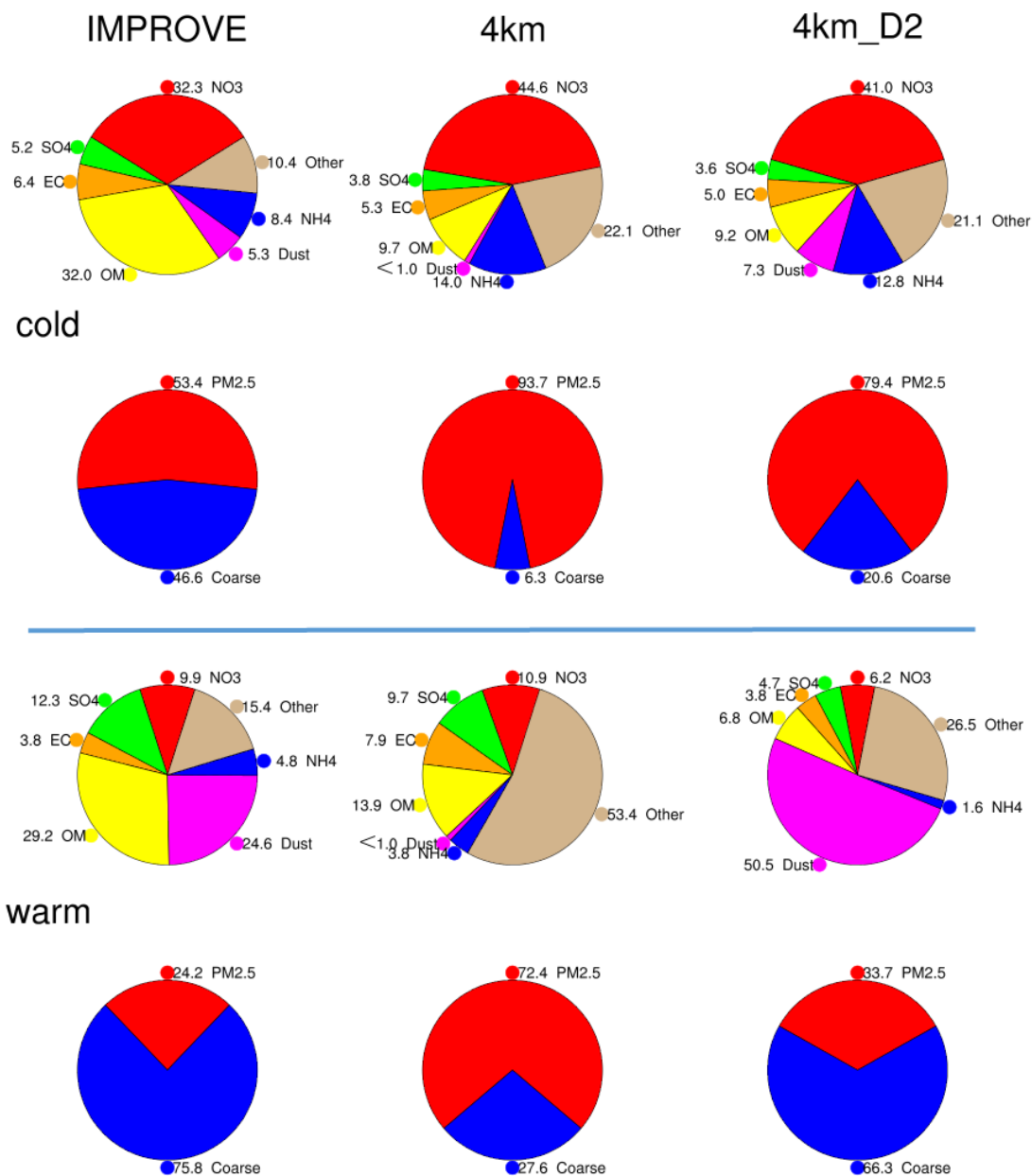
903

904 Figure 8. Mean dust emission rate ($\mu\text{g m}^{-2} \text{s}^{-1}$) from the 4km and 4km_D2 runs.



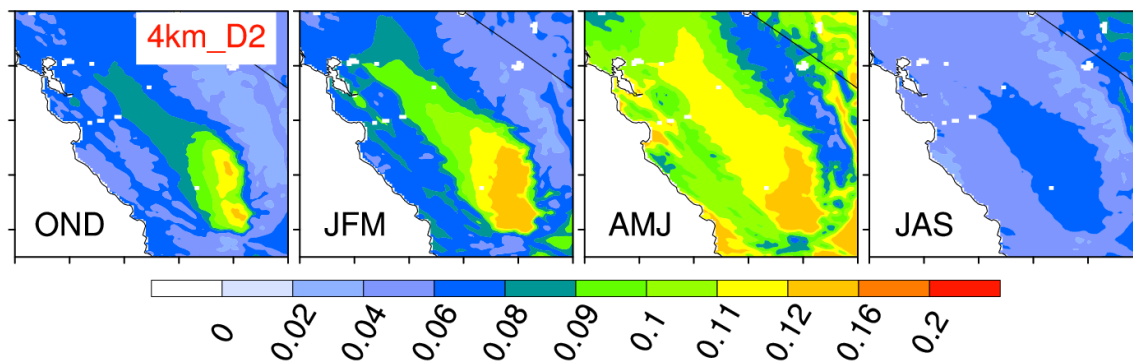
905

906 Figure 9. Fraction of erodible surface in the GOCART dataset used in this study.



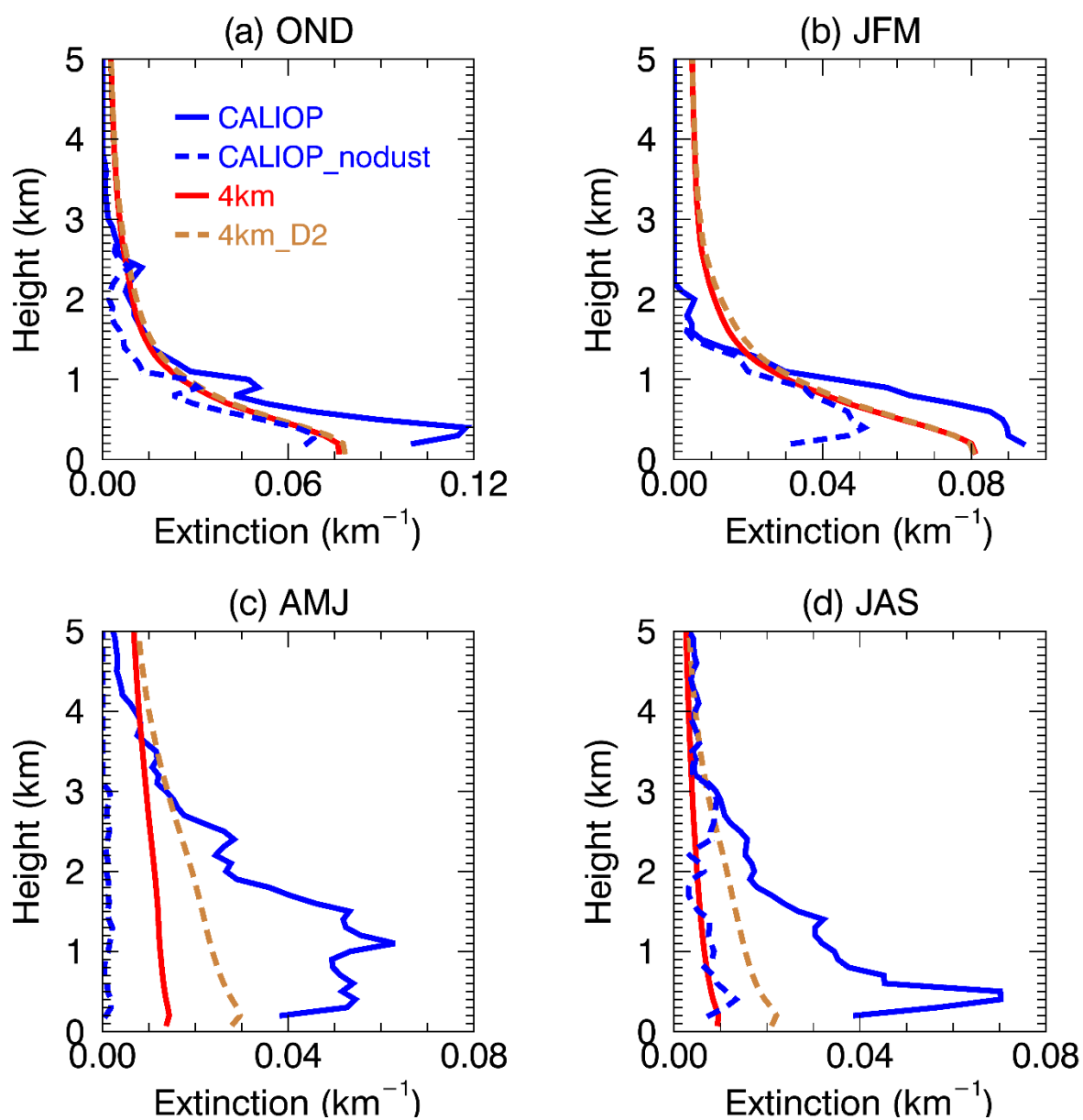
907

908 Figure 10. Relative contribution (%) of aerosol species from IMPROVE and the WRF-Chem (4km
 909 and 4km_D2) simulations at Fresno, CA in WY2013. (Panel 1) Contribution to PM_{2.5} in the cold
 910 season; (Panel 2) relative contribution of PM_{2.5} and coarse mass (CM) to PM₁₀ in the cold season;
 911 (Panel 3) same as Panel 1 but in the warm season; (Panel 4) same as Panel 2 but in the warm season.
 912 “Other” refers to the difference of PM_{2.5} total mass and specified PM_{2.5} (NO₃, NH₄, OM, EC, SO₄
 913 and dust).



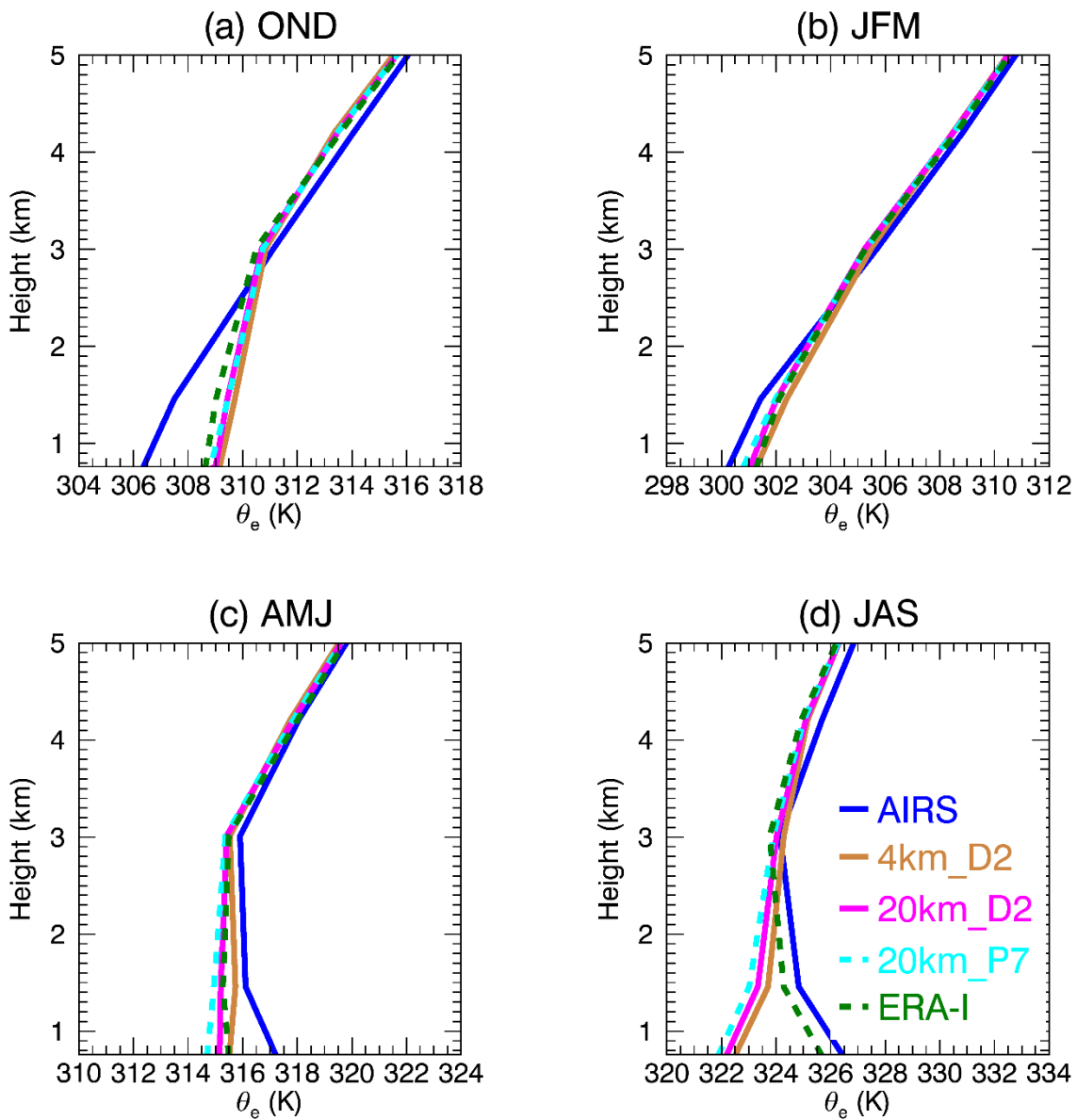
914

915 Figure 11. Spatial distribution of seasonal mean 550 nm AOD from the 4km_D2 run in WY2013.



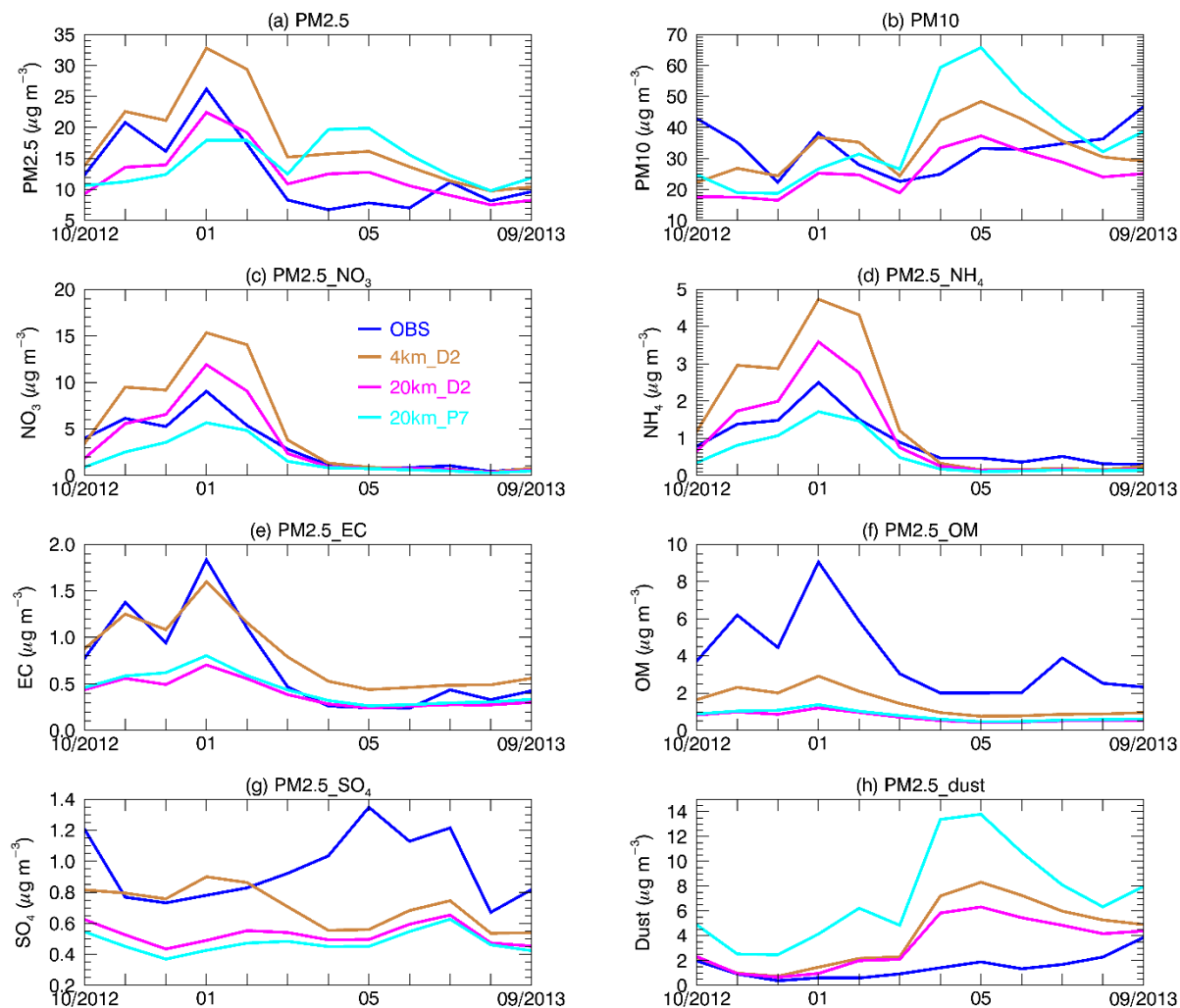
916

917 Figure 12. Vertical distribution of seasonal mean 532 nm aerosol extinction coefficient (km^{-1})
 918 from CALIOP (blue) and the WRF-Chem (4km and 4km_D2) simulations over the red box
 919 region in Fig. 1a in WY2013. Blue dashed lines (CALIOP_nodust) represent the CALIOP
 920 profiles without dust (dust and polluted dust).

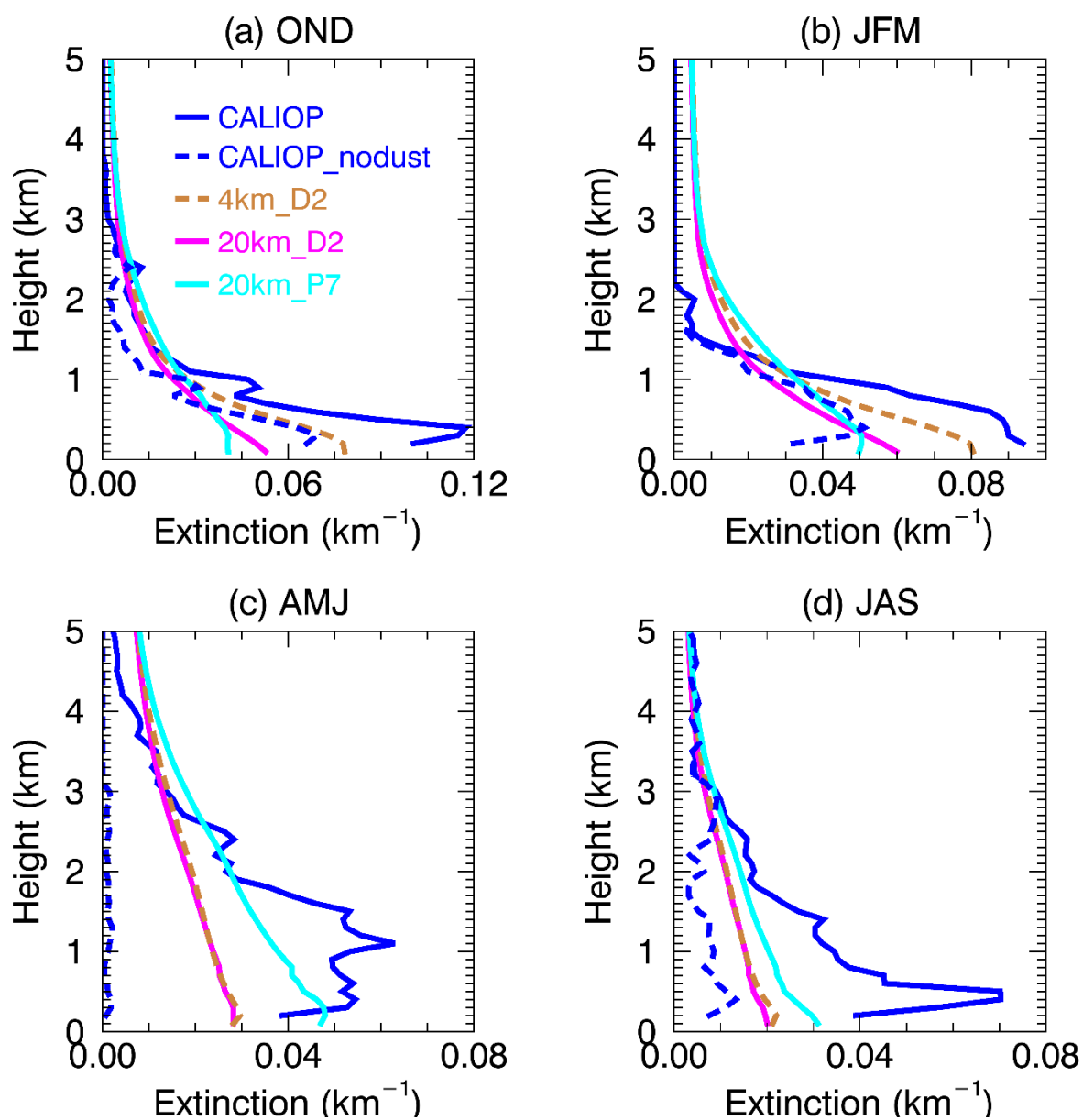


921

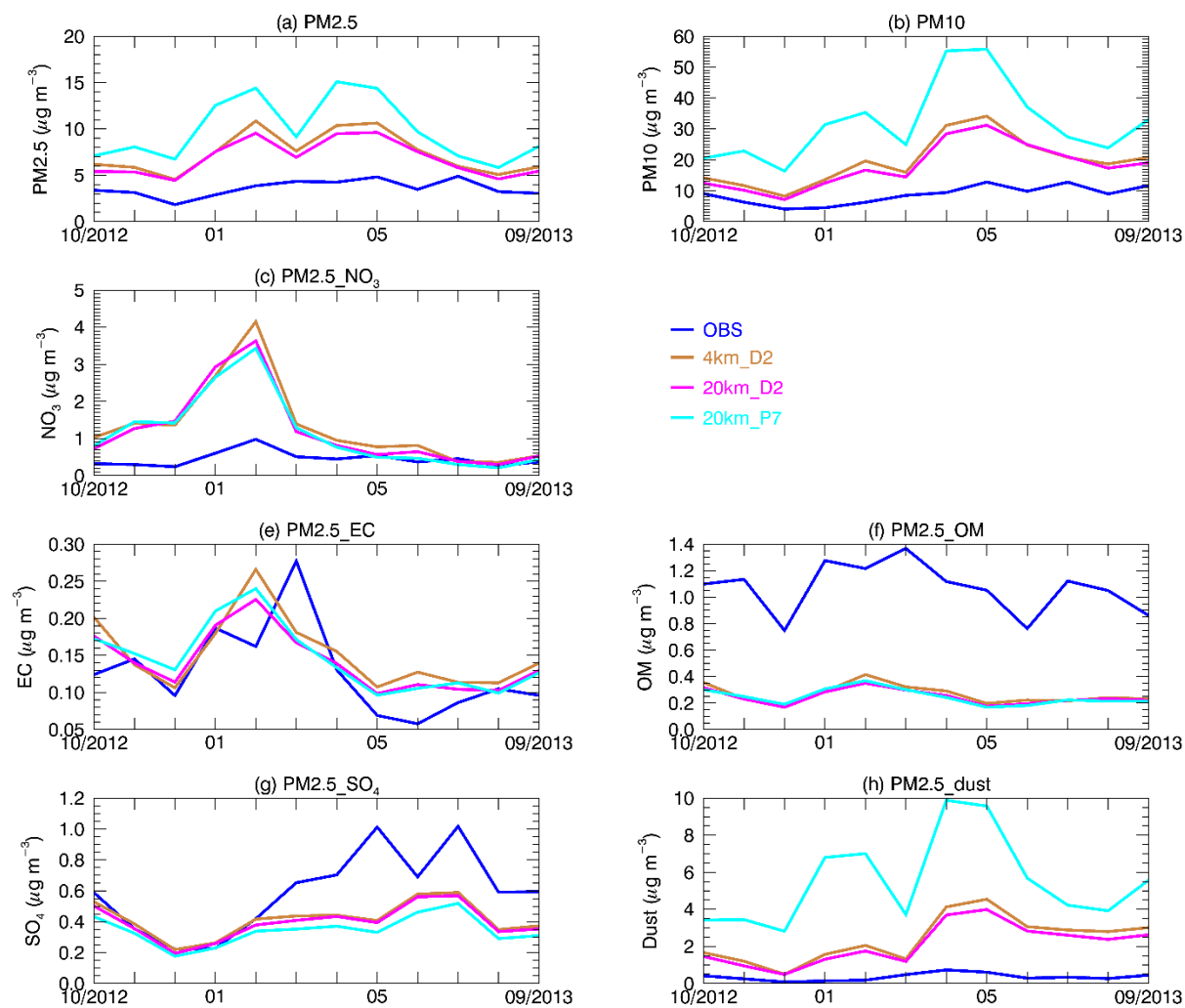
922 Figure 13. Vertical distribution of season mean equivalent potential temperature (θ_e ; K) from AIRS,
 923 ERA-Interim (ERA-I) and the WRF-Chem (4km_D2, 20km_D2 and 20km_P7) simulations over
 924 the red box region in Fig. 1a in WY2013. The 4km run (not shown) is similar to the 4km_D2 run.



925
 926 Figure 14. Aerosol mass ($\mu\text{g m}^{-3}$) for different species from OBS, the 4km_D2, 20km_D2 and
 927 20km_P7 simulations at Fresno, CA. NH_4 observations are from EPA; other observations are from
 928 IMPROVE. $\text{PM}_{2.5_NO_3}$ represents NO_3 with diameter $\leq 2.5 \mu\text{m}$. Similar definition for NH_4 , EC,
 929 OM, SO_4 and dust in the figures.

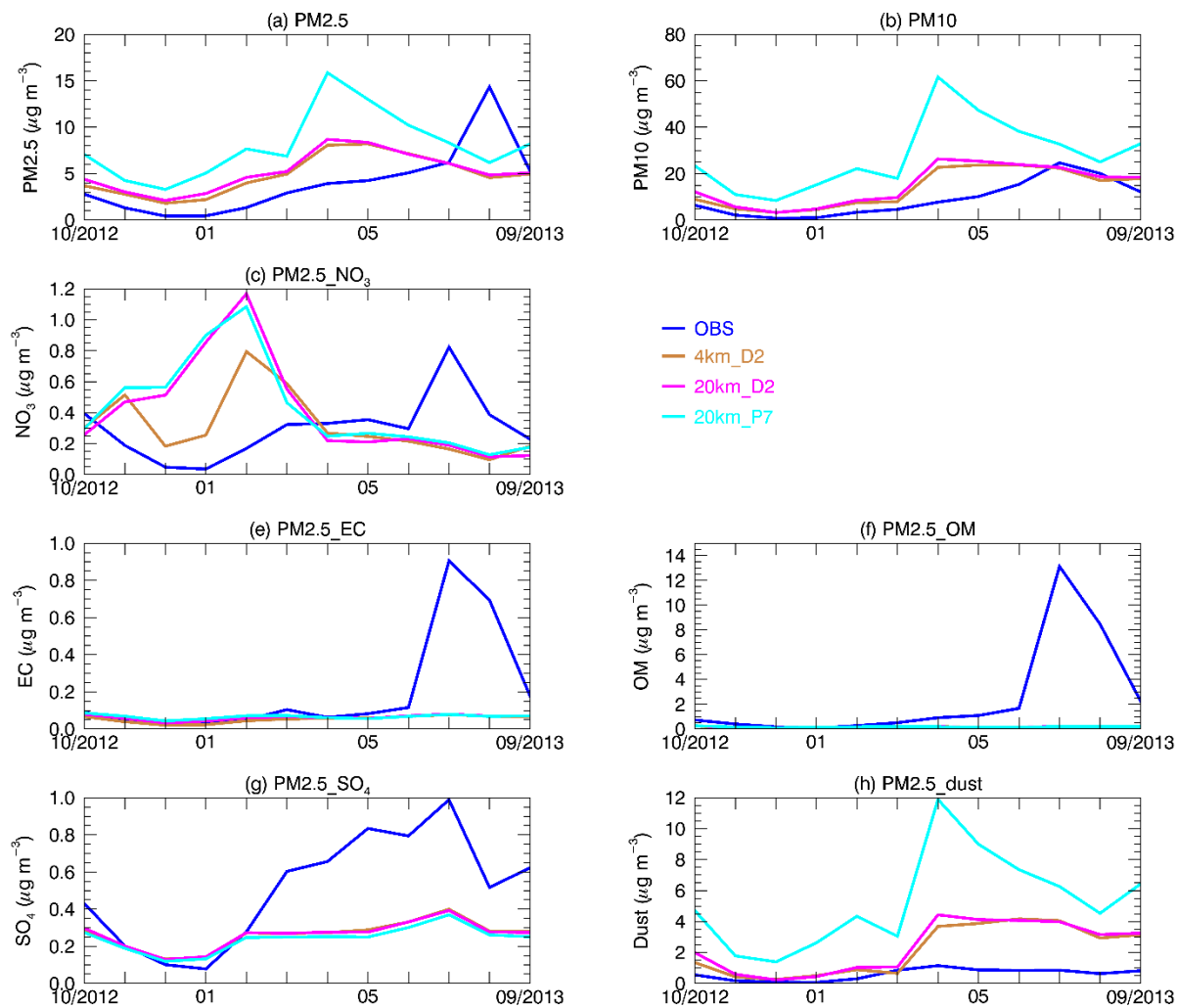


930
 931 Figure 15. Vertical distribution of seasonal mean 532 nm aerosol extinction coefficient (km^{-1})
 932 from CALIOP, CALIOP_nodust, and the WRF-Chem (4km_D2, 20km_D2 and 20km_P7)
 933 simulations over the red box region in Fig. 1a in WY2013.



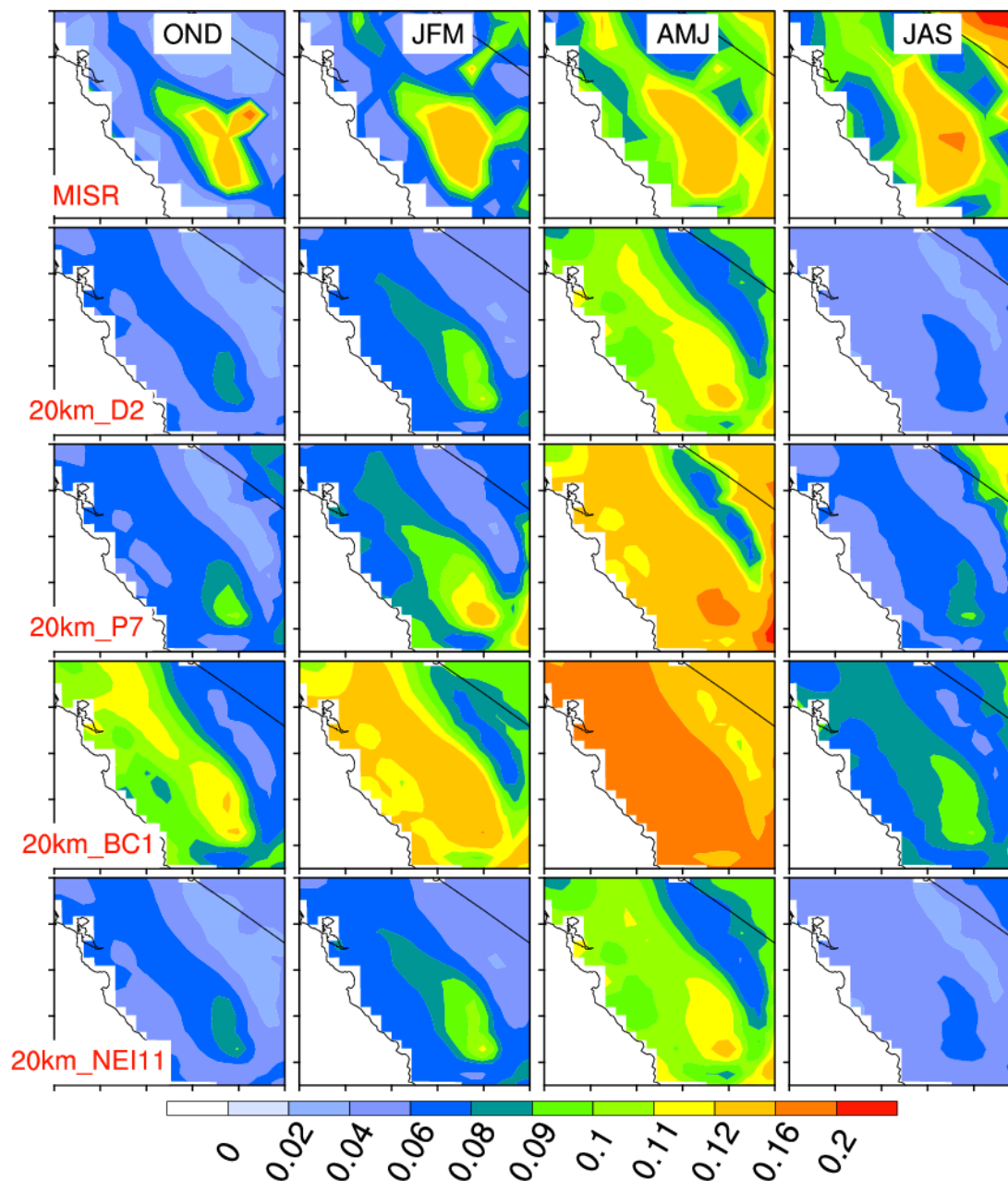
934

935 Figure 16. Aerosol mass ($\mu\text{g m}^{-3}$) for different species from IMPROVE (OBS), the 4km_D2,
 936 20km_D2 and 20km_P7 simulations at Pinnacles, CA.



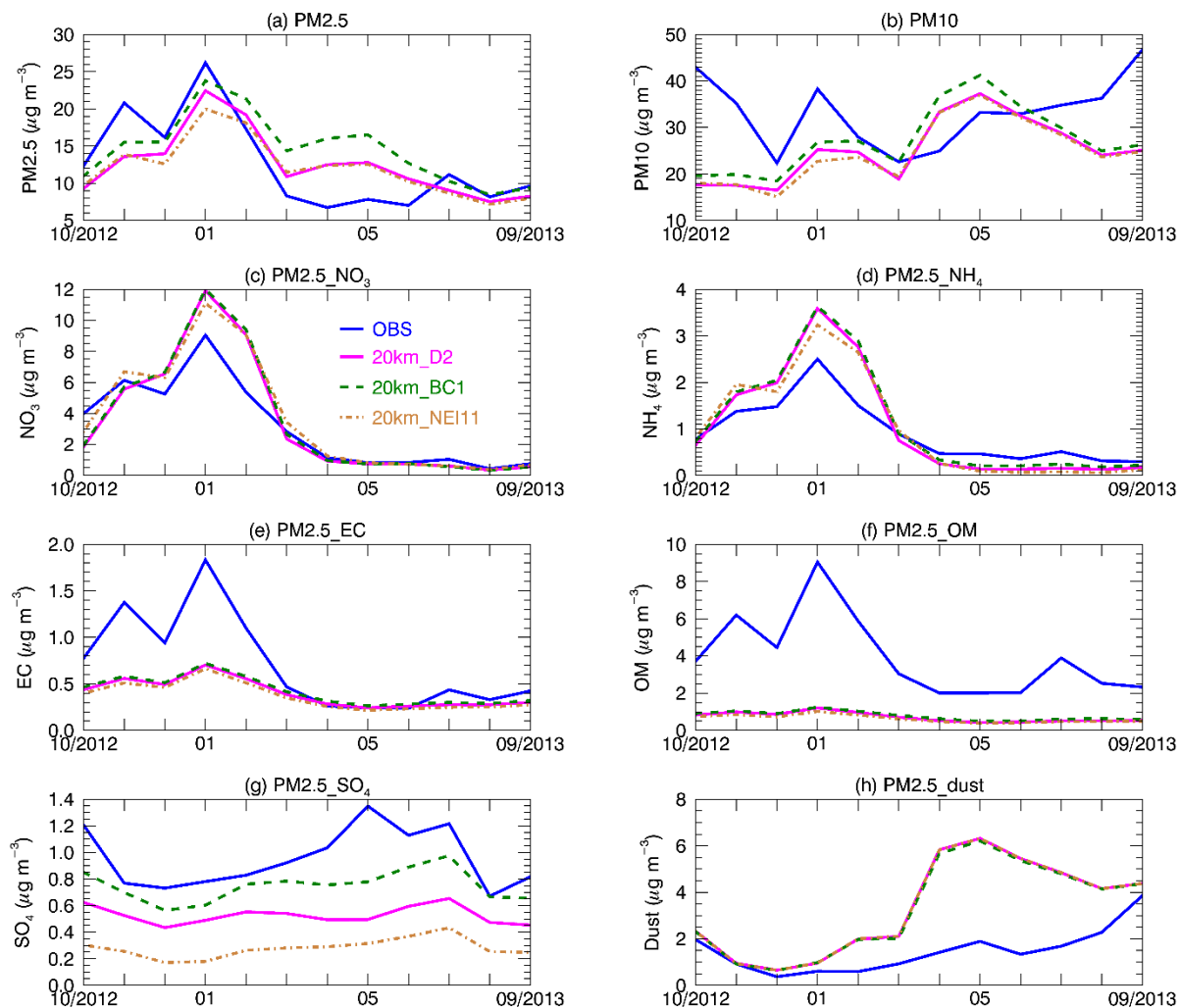
937

938 Figure 17. Aerosol mass ($\mu\text{g m}^{-3}$) for different species from IMPROVE (OBS), the 4km_D2,
 939 20km_D2 and 20km_P7 simulations at Kaiser, CA.

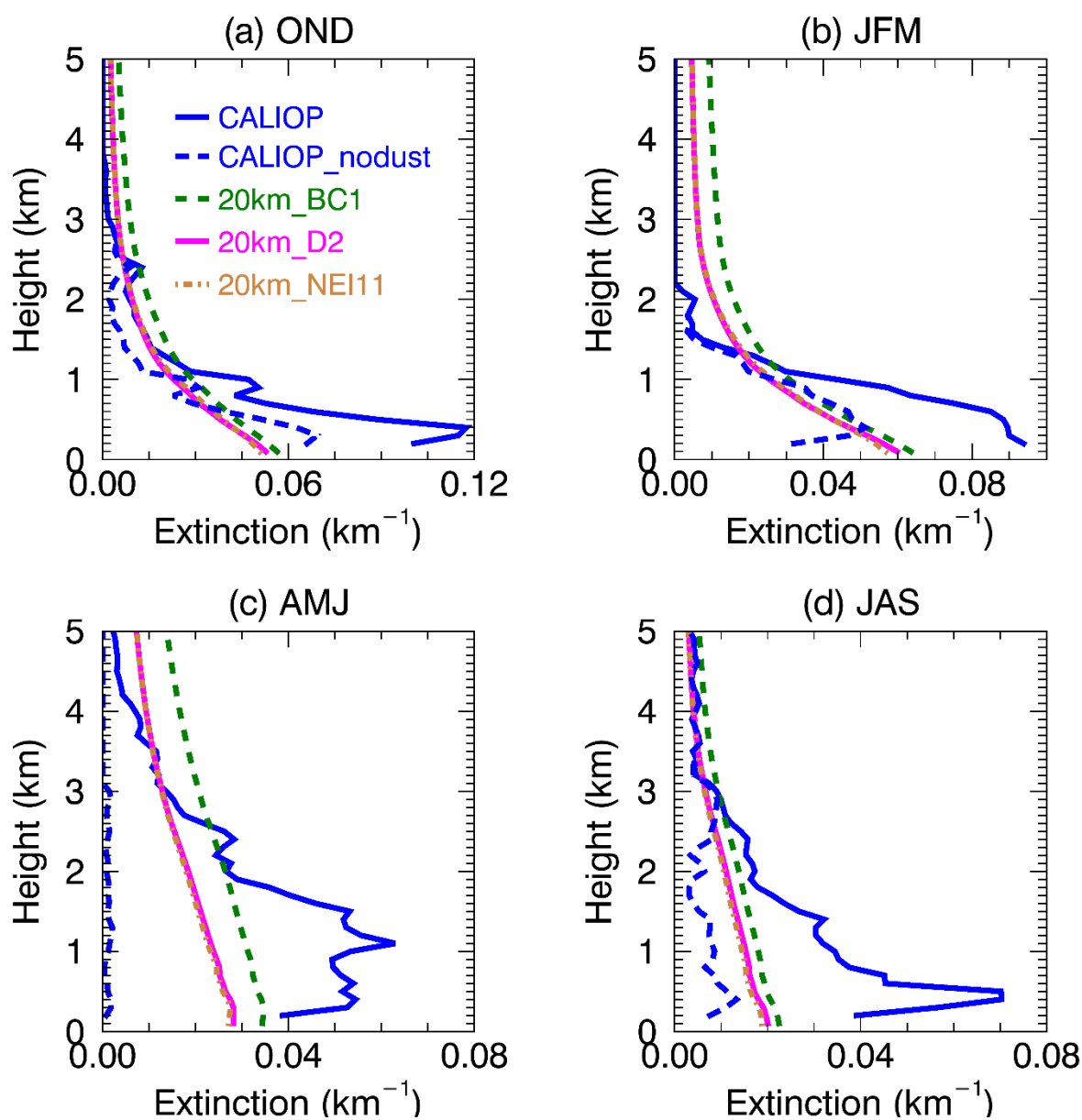


940

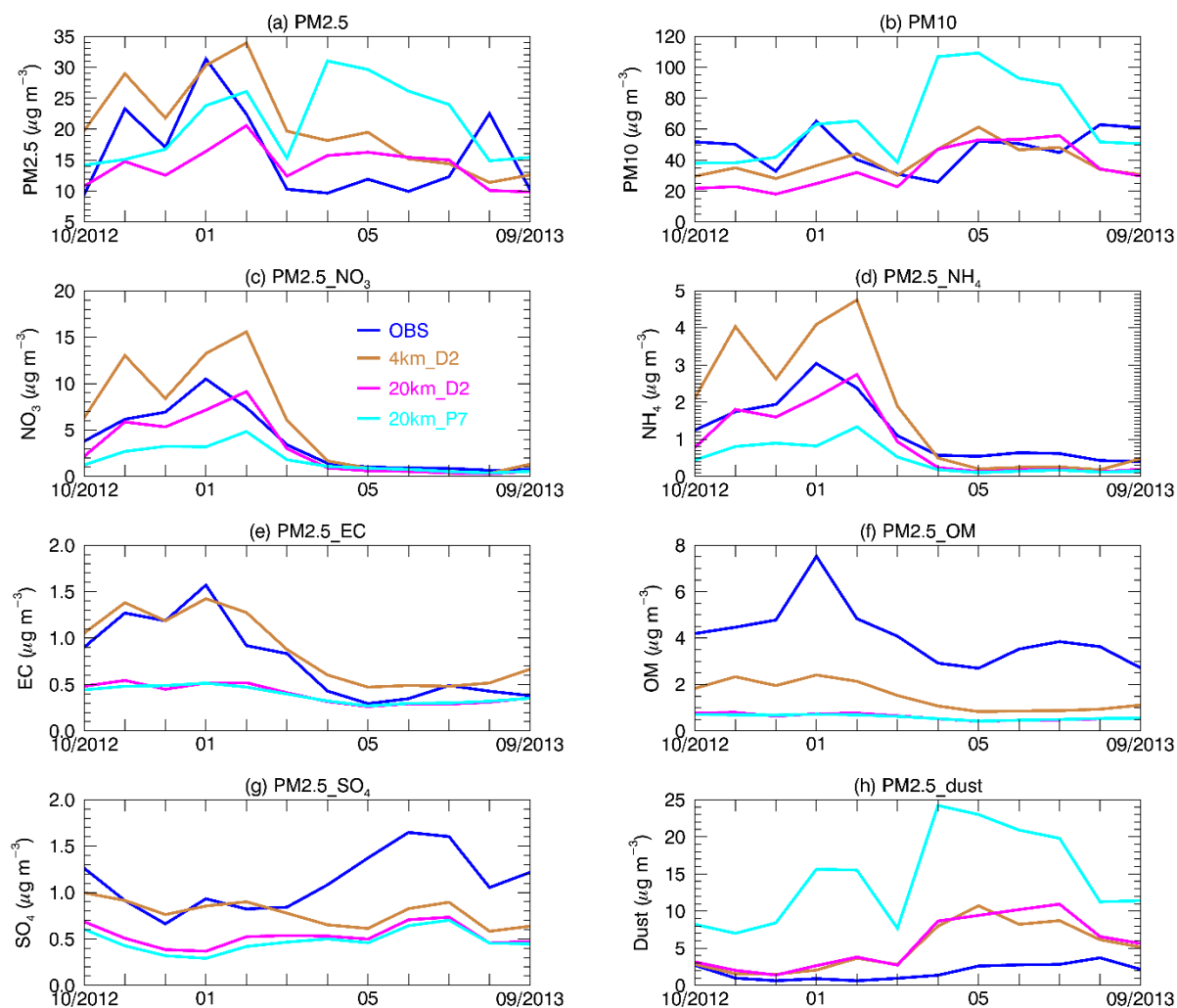
941 Supplementary Figure 1. Spatial distribution of seasonal mean 550 nm AOD from MISR and the
 942 WRF-Chem (20km_D2, 20km_P7, 20km_BC1 and 20km_NEI11) simulations in WY2013. OND:
 943 October-November-December; JFM: January-February-March; AMJ: April-May-June; JAS: July-
 944 August-September. The 20km_BC1 run is the same as the 20km_D2 run except that chemical
 945 boundary conditions use MOZART-4 original data. The 20km_NEI11 run is the same as the
 946 20km_D2 run except with NEI11 anthropogenic emissions.



947
 948 Supplementary Figure 2. Aerosol mass ($\mu\text{g m}^{-3}$) for different species from OBS, the 20km_D2,
 949 20km_BC1 and 20km_NEI11 simulations at Fresno, CA. NH_4 observations are from EPA; other
 950 observations are from IMPROVE. $\text{PM}_{2.5_}\text{NO}_3$ represents NO_3 with diameter $\leq 2.5 \mu\text{m}$. Similar
 951 definition for NH_4 , EC, OM, SO_4 and dust in the figures.

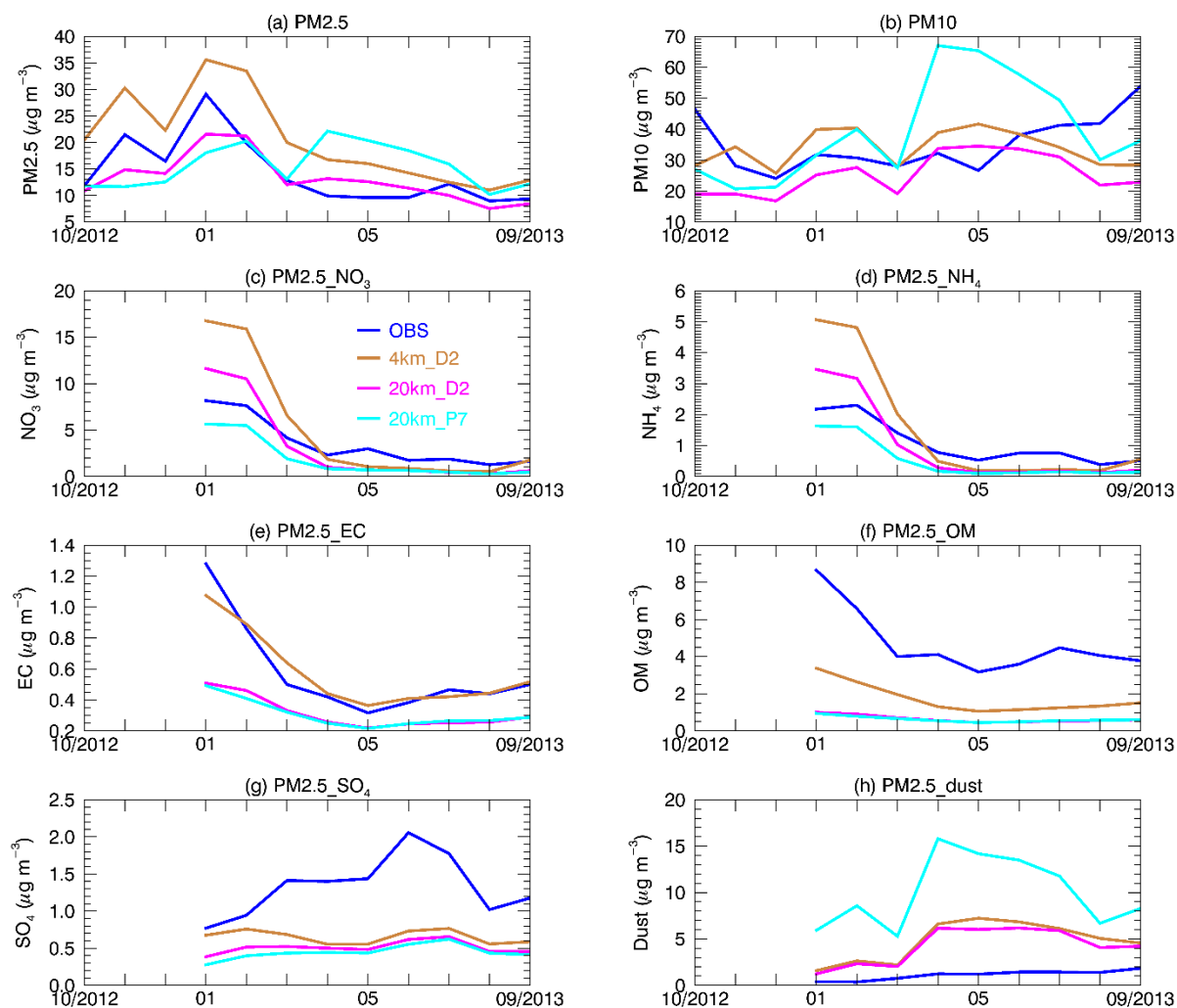


952
 953 Supplementary Figure 3. Vertical distribution of seasonal mean 532 nm aerosol extinction
 954 coefficient (km^{-1}) from CALIOP, CALIOP_nodust, and the WRF-Chem (20km_D2, 20km_BC1
 955 and 20km_NEI11) simulations over the red box region in Fig. 1a in WY2013.



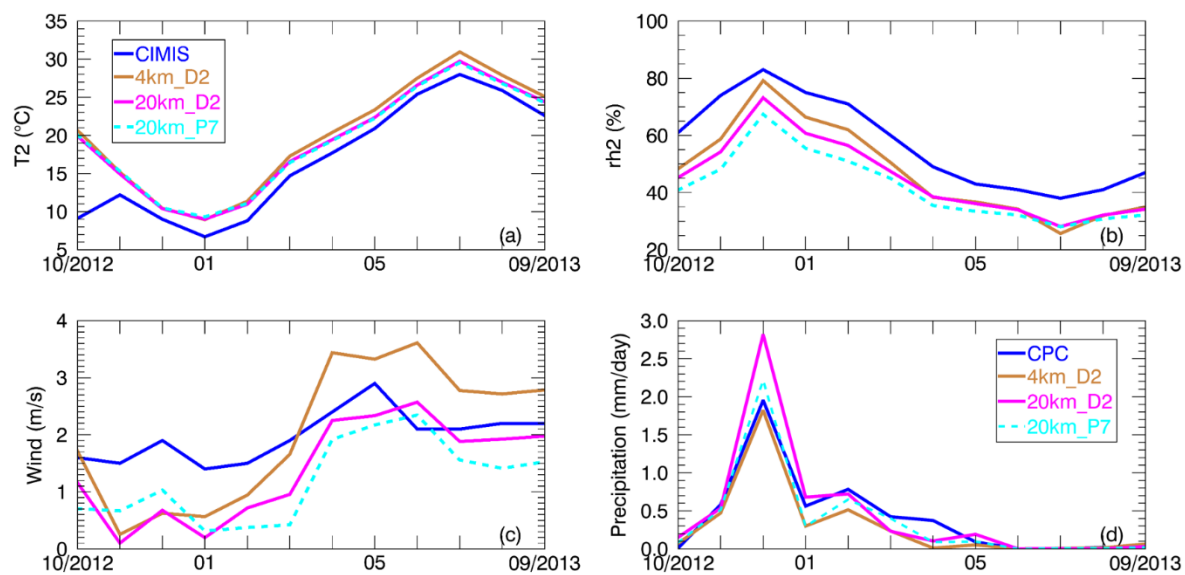
956

957 Supplementary Figure 4. Aerosol mass ($\mu\text{g m}^{-3}$) for different species from EPA CSN (OBS), the
 958 4km_D2, 20km_D2 and 20km_P7 simulations at Bakersfield, CA. PM_{2.5}_NO₃ represents NO₃
 959 with diameter $\leq 2.5 \mu\text{m}$. Similar definition for SO₄, EC, OM, NH₄ and dust in the figures.

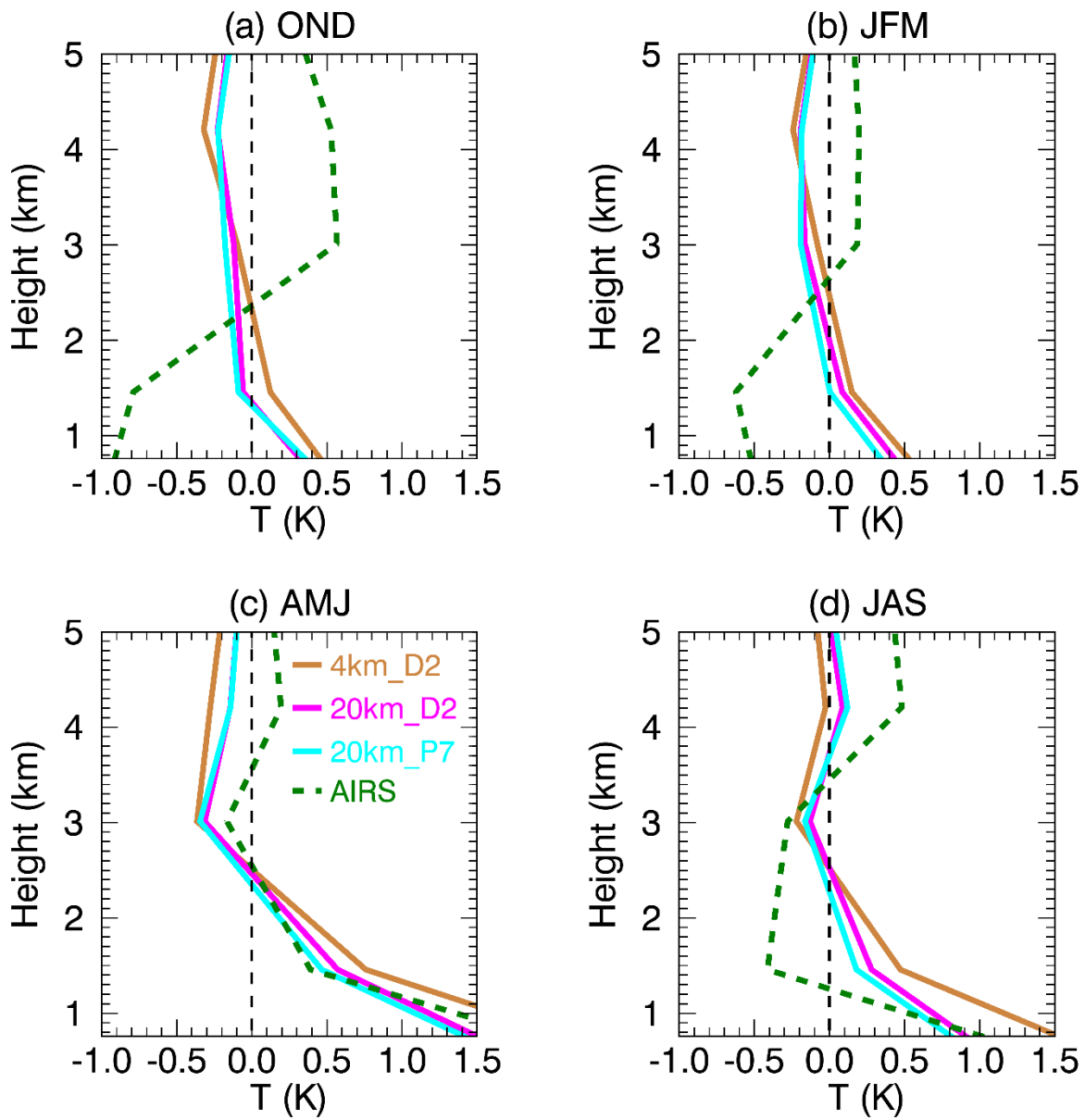


960

961 Supplementary Figure 5. Aerosol mass ($\mu\text{g m}^{-3}$) for different species from EPA CSN (OBS), the
 962 4km_D2, 20km_D2 and 20km_P7 simulations at Modesto, CA.

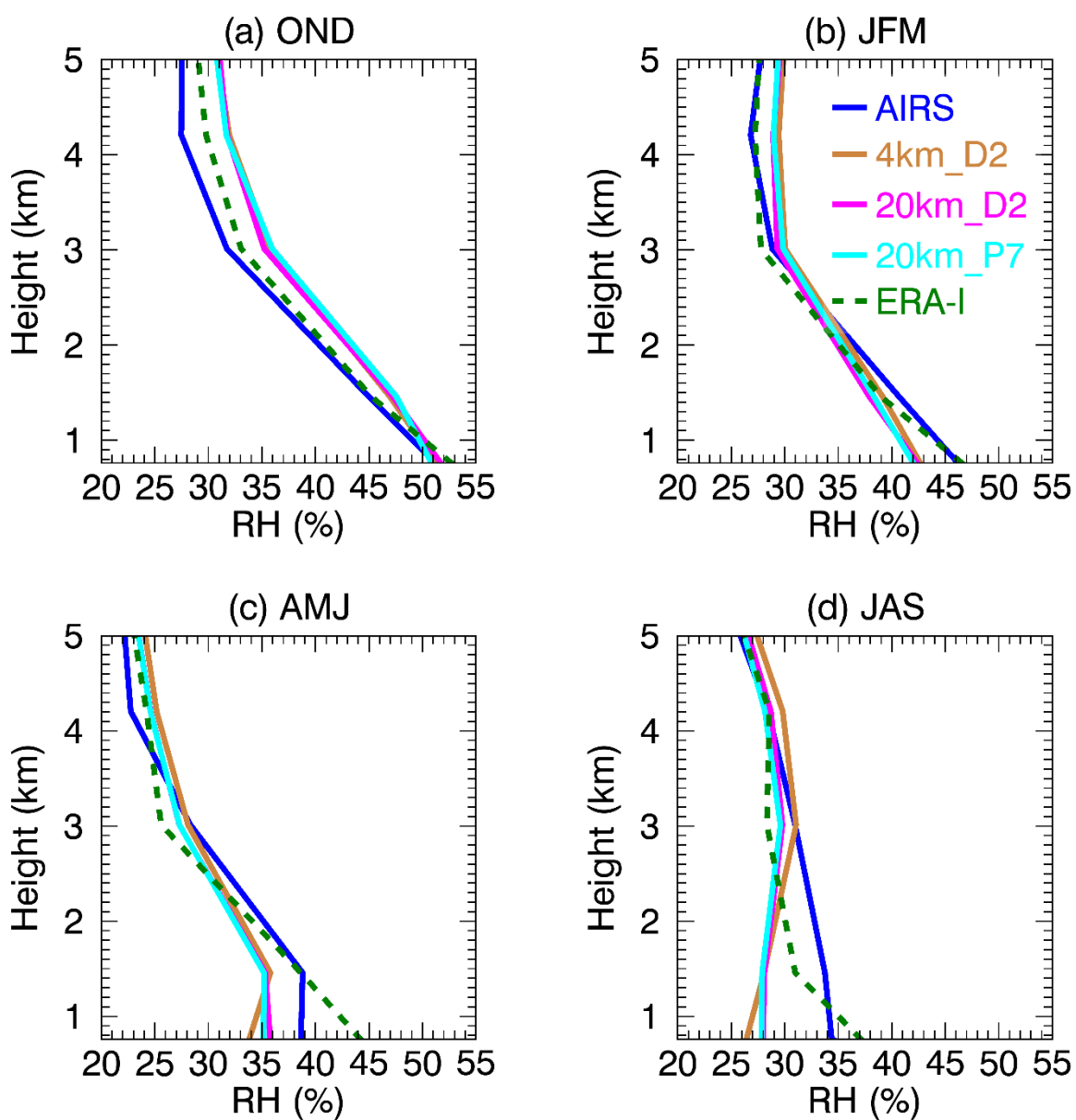


963
 964 Supplementary Figure 6. Monthly mean of (a) 2-m temperature ($^{\circ}\text{C}$); (b) 2-m relative humidity
 965 (%); (c) 10-m wind speed (m/s); (d) precipitation (mm/day) at Fresno, CA. The 20km (not shown)
 966 run is similar to the 20km_D2 run while the 4km (not shown) run is similar to the 4km_D2 run.

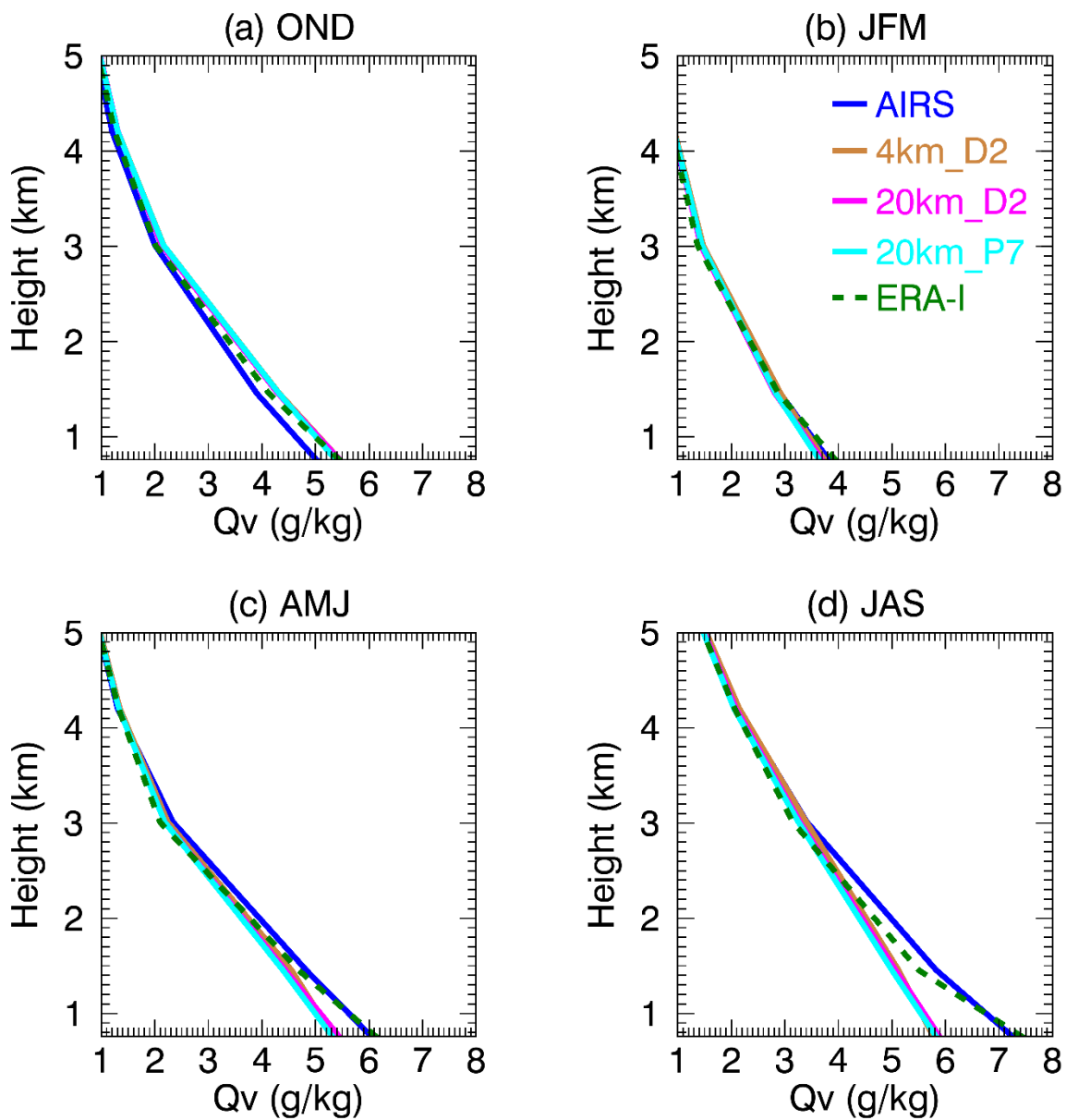


967

968 Supplementary Figure 7. Vertical profile of seasonal mean temperature (K) bias in the WRF-Chem
 969 simulations and AIRS comparing to ERA-Interim. The 20km run (not shown) is similar to the
 970 20km_D2 run while the 4km run (not shown) is similar to the 4km_D2 run.



971
 972 Supplementary Figure 8. Vertical profile of seasonal mean relative humidity (%) in the WRF-Chem
 973 simulations, AIRS and ERA-Interim. The 20km run (not shown) is similar to the 20km_D2 run
 974 while the 4km run (not shown) is similar to the 4km_D2 run.



975
 976 Supplementary Figure 9. Vertical profile of seasonal mean specific humidity (g kg^{-1}) in the WRF-
 977 Chem simulations, AIRS and ERA-Interim. The 20km run (not shown) is similar to the 20km_D2
 978 run while the 4km run (not shown) is similar to the 4km_D2 run.